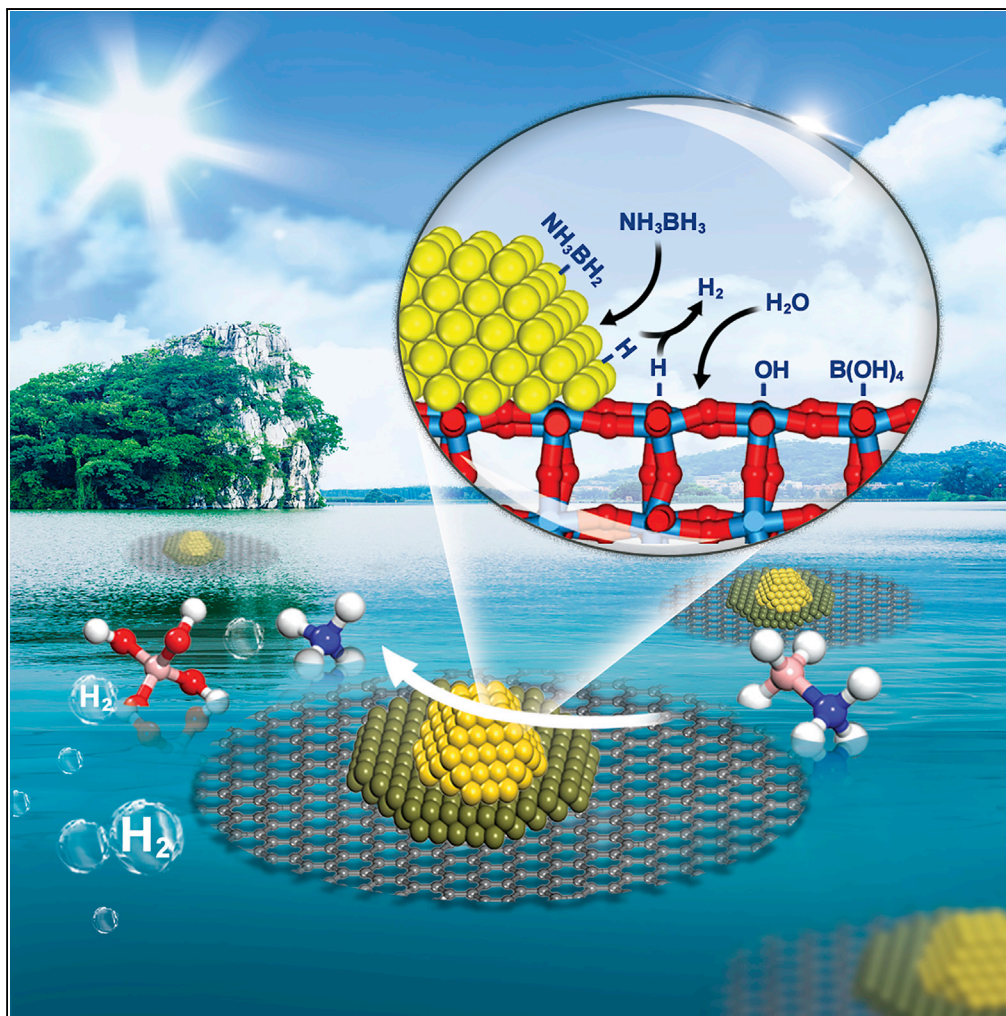


Article

Synergistic Pt-WO₃ Dual Active Sites to Boost Hydrogen Production from Ammonia Borane

Wenyao Chen,
Wenzhao Fu,
Gang Qian,
Bingsen Zhang,
De Chen, Xuezhi
Duan, Xingguo
Zhou

xzduan@ecust.edu.cn

HIGHLIGHTS

Mechanism-guided
design of Pt-WO₃ dual
active sites boosts H₂
generation

A trade-off between WO₃
loading and Pt B.E. yields
a volcano-shaped activity

WO₃ acts as the sacrificial
site to divert by-products
against deactivation

Multifunctional Pt-MO/C
catalysts achieve
enhanced activity and
durability

Chen et al., iScience 23,
100922
March 27, 2020 © 2020 The
Authors.
[https://doi.org/10.1016/
j.isci.2020.100922](https://doi.org/10.1016/j.isci.2020.100922)

Article

Synergistic Pt-WO₃ Dual Active Sites to Boost Hydrogen Production from Ammonia BoraneWenyao Chen,¹ Wenzhao Fu,¹ Gang Qian,¹ Bingsen Zhang,² De Chen,³ Xuezhi Duan,^{1,4,*} and Xinggui Zhou¹

SUMMARY

Development of synergistic heterogeneous catalysts with active sites working cooperatively has been a pursuit of chemists. Herein, we report for the first time the fabrication and manipulation of Pt-WO₃ dual-active-sites to boost hydrogen generation from ammonia borane. A combination of DFT calculations, structural characterization, and kinetic (isotopic) analysis reveals that Pt and WO₃ act as the active sites for ammonia borane and H₂O activation, respectively. A trade-off between the promoting effect of WO₃ and the negative effect of decreased Pt binding energy contributes to a volcano-shaped activity, and Pt/CNT-5W delivers a 4-fold increased activity of 710.1 mol_{H₂} · mol_{Pt}⁻¹ · min⁻¹. Moreover, WO₃ is suggested to simultaneously act as the sacrificial site that can divert B-containing by-products away from Pt sites against deactivation, yielding an increase from 24% to 68% of the initial activity after five cycles. The strategy demonstrated here could shed a new light on the design and manipulation of dual-active-site catalysts.

INTRODUCTION

Noble metal catalysts are the workhorses for energy and environment applications, which enable the conversion of feedstock molecules to desired products (Pakhare and Spivey, 2014; Zhou et al., 2010). Nevertheless, their expenses and scarcity limit the viability for large-scale commercialization (Wu et al., 2011; Gong et al., 2012). Continuous efforts have been devoted to engineering the noble metal catalysts by tailoring their sizes, shapes, and compositions to improve the metal utilization efficiency and ultimately the catalytic performance (Aijaz et al., 2012; Zhang et al., 2009; Zecevic et al., 2013). Generally, the supported noble metal catalysts are often chemically and physically complex due to their multi-elemental, porous, and hierarchically structured natures, rendering their rational design and manipulation extremely challenging (Meirer and Weckhuysen, 2018; Yu et al., 2012; Shrestha et al., 2011). Fortunately, with the rapid development of computational chemistry, (micro) kinetics analysis, multiple characterization, isotope experiments, etc., it endows us with great opportunities to explore the reaction mechanism and kinetics with judicious interpretation of their results and then design highly efficient noble metal catalysts (Allian et al., 2011; Aramouni et al., 2018; Chin et al., 2011; Dasgupta et al., 2013; Hmadeh et al., 2014; Norskov et al., 2011; Pan and Bao, 2011; Qiao et al., 2011; Wu et al., 2012; Yamada et al., 2011).

Hydrogen is a well-known ideal energy carrier, and its safe and efficient storage as well as facile release is the key toward a hydrogen economy (Moussa et al., 2013; Turner, 2004; Diwan et al., 2011; Diakov et al., 2007; Demirkan et al., 2019; Sogut et al., 2019; Sen et al., 2018). With high hydrogen content (19.6 wt%), long-term stability, and nontoxicity at room temperature, ammonia borane (NH₃BH₃, AB) has been regarded as a promising hydrogen storage material (Yan et al., 2008; Valero-Pedraza et al., 2019; Yao et al., 2016; Li et al., 2017; Metin et al., 2010). Although a fast evolution of hydrogen from ammonia borane hydrolysis has been demonstrated by using noble metal catalyst, especially Pt and Ru, optimizing its activity and durability to minimize its usage is still of paramount importance (Zhang et al., 2017, 2018; Akbayrak and Ozkar, 2012; Mori et al., 2016; Yan et al., 2017). Some studies have identified the interactions between Pt surface and H atom within ammonia borane and its resultant formation of activated complex species as the prerequisite to generate hydrogen (Chen et al., 2017a; Yang et al., 2011). To this end, it is highly desirable to engineer the properties of metal and substrate through two main approaches. One is alloying with other components to integrate multi-components with different properties (Wang et al., 2014; Zhang et al., 2009; Chen et al., 2017b). The other is tailoring the surface chemistry of catalyst support to obtain the targeted properties of supported metal (Chen et al., 2014, 2015, 2018; Khalily et al., 2016; Lara et al., 2019).

¹State Key Laboratory of Chemical Engineering, East China University of Science and Technology, 130 Meilong Road, Shanghai 200237, China

²Shenyang National Laboratory for Materials Science, Institute of Metal Research, Chinese Academy of Sciences, 72 Wenhua Road, Shenyang 110016, China

³Department of Chemical Engineering, Norwegian University of Science and Technology, 7491 Trondheim, Norway

⁴Lead Contact

*Correspondence: xzduan@ecust.edu.cn

<https://doi.org/10.1016/j.isci.2020.100922>



Notably, rational catalyst design relies on understanding of the mechanism by which catalysts operate. Our recent studies on the kinetics and reaction mechanism of Pt-catalyzed ammonia borane hydrolysis (Chen et al., 2017a) indicate that the Pt catalyst displays a good capacity to dissociate the B–H bond within ammonia borane, but it is intrinsically inactive to dissociate the O–H bond within H₂O, and the NH₃BH₂* assisted dissociation of O–H bond within H₂O*, i.e., NH₃BH₂*+H₂O* → NH₃BH₂(OH)*+H* as the rate-determining step (RDS). Moreover, DFT calculations reveal that pure Pt metal surface binds H₂O too weakly to dissociate H₂O, whereas some transition metal oxides exhibit great potentials for facile H₂O dissociation (Ishikawa et al., 2002; Yang et al., 2017). Consequently, it is reasonable to assume that fabricating Pt-metal oxide synergistic catalyst with active sites working cooperatively could pave an effective way for hydrogen generation.

In addition to the hydrogen generation activity, the catalyst durability is another important criterion to evaluate the performance of metal catalysts, often more critical for noble metal catalysts. Our previous studies on highly active carbon-supported Pt catalysts have shown that the catalyst deactivation mainly arises from the agglomeration of Pt nanoparticles and the adsorption of poisonous B-containing by-products on the catalyst surfaces during the reaction (Chen et al., 2014b, 2015). Based on the reaction and deactivation mechanisms, tailoring Pt particle sizes and distributions as well as introducing more oxygen-containing groups and defects onto the carbon support surfaces has been demonstrated to effectively suppress the Pt agglomeration and/or to increase the Pt binding energy for the inhibited poison adsorption (Chen et al., 2014b, 2015; Zhang et al., 2017). Considering that introduction of metal oxides could help stabilize noble metal nanoparticles (Cao et al., 2010) and adsorb anions (Sverjensky and Fukushi, 2006), an attempt would be highly desirable to design Pt-metal oxide multi-functional catalyst by employing the metal oxide to act as anchoring and sacrificial sites against deactivation, thus not only enhancing the hydrogen generation activity mentioned above but also improving the catalyst durability.

Herein, we report a strategy to design and fabricate dual-active-site catalysts to boost hydrogen production from ammonia borane hydrolysis. DFT calculations were first carried out to assist the fabrication of Pt-WO₃ dual-active-site synergistic catalyst. Along this line, a series of tungsten-incorporated CNT-γW were prepared to immobilize Pt particles with the same loading. Catalytic activity and durability tests were performed to explore the promotion effects of WO₃ on the catalytic performance. A combination of comprehensive characterizations, kinetic (isotopic) investigations, and DFT calculations was employed to reveal the structure-performance relationship, and a dual-active-site mechanism was proposed to contribute to the simultaneously enhanced activity and durability. This provides a feasible avenue to design and develop dual-active-site catalysts by combining theoretical and experimental studies in this research area.

RESULTS

DFT-Assisted Catalyst Design and Fabrication of CNT-γW

As discussed above, fabricating Pt-metal oxide might be an effective strategy to obtain synergistic catalyst, with dual active sites working cooperatively for the activation of ammonia borane and H₂O. Exemplified with WO₃, the adsorption and activation of ammonia borane and H₂O on the representative WO₃(100) and Pt(111) surfaces, as the thermodynamically stable and most exposed facets (Hurtado-Aular et al., 2020; Mahata and Pathak, 2017), were comparatively studied by DFT calculations. The optimized most stable adsorption configurations of the involved species on Pt(111) and WO₃(100) surfaces are listed in Figure S1, and the corresponding potential energy profiles are displayed in Figures 1A and 1B, respectively. It can be obviously observed in Figure 1A that the ammonia borane dissociatively adsorbs on the Pt(111) surface, in comparison with the much higher activation barrier of 1.67 eV over the WO₃(100) surface. This indicates that the Pt site facilitates the activation of ammonia borane with respect to the WO₃ site. In contrary, the WO₃ site (i.e., 0.11 eV) shows much lower activation barrier for H₂O dissociation than the Pt site (i.e., 0.83 eV) as shown in Figure 1B, in consistent with the larger H–O bond elongation over the WO₃(100) surface as shown in Figure S1. Therefore, it can be theoretically predicted that fabricating Pt-WO₃ dual sites for acting as a synergistic catalyst can promote ammonia borane hydrolysis.

Considering that the low specific surface area of WO₃ is unfavorable for Pt immobilization (Jin et al., 2017), carbon nanotube (CNT) with high external surface area, close ends, and mesoporous structure (Chen et al., 2014b, 2015) was employed as the catalyst support to enhance the specific surface area of WO₃ by incorporating WO₃ onto CNT for the following Pt immobilization. Specifically, the tungsten-incorporated supports were prepared by mixing pristine CNT with ammonium tungstate aqueous solutions of different

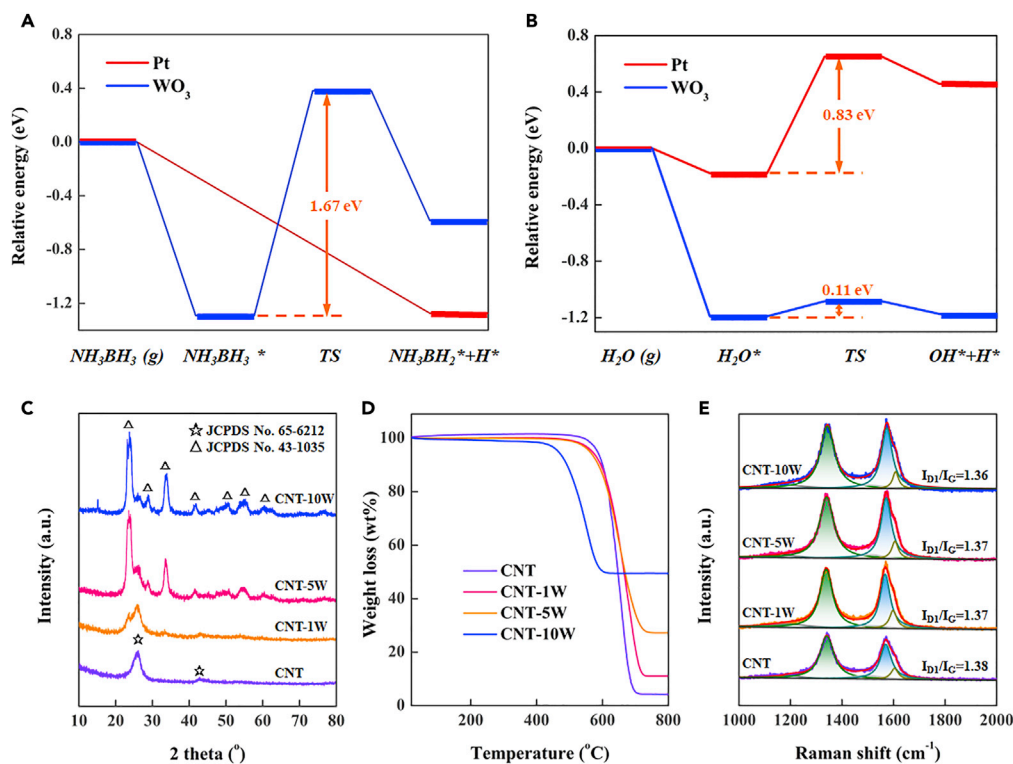


Figure 1. DFT Calculations of Ammonia Borane and H₂O Activation as well as Structural Characterization of CNT- γ W

(A) Potential energy diagrams of ammonia borane activation over Pt(111) and WO₃(100) surfaces.

(B) Potential energy diagrams of H₂O activation over Pt(111) and WO₃(100) surfaces.

(C) XRD patterns of CNT, CNT-1W, CNT-5W, and CNT-10W.

(D) TGA profiles of CNT, CNT-1W, CNT-5W, and CNT-10W.

(E) Raman spectra of CNT, CNT-1W, CNT-5W, and CNT-10W.

concentrations (i.e., 1, 5 and 10 wt%) at 90°C for 10 h, followed by filtering, washing, drying, and calcination under Ar at 450°C for 2 h. The as-obtained samples were denoted as CNT- γ W, in which γ represents the concentration of ammonium tungstate aqueous solution. X-ray diffraction (XRD) spectra in Figure 1C show that, after the incorporation of WO₃, the CNT- γ W samples exhibit some distinct characteristic diffraction peaks of WO₃ (JCPDS No. 43-1035), in addition to the two characteristic diffraction peaks of graphite (JCPDS No. 65-6212) from the CNT. Notably, these diffraction peaks become intensive and sharp with the concentration of ammonium tungstate solution, indicating the increased amount and size of WO₃ particles over the CNT- γ W.

Thermal gravimetric analysis (TGA) was further carried out to determine the loadings of WO₃ over the CNT- γ W. As shown in Figure 1D, the residue weight of pristine CNT is estimated around 3.0 wt% originating from the metal catalyst of CNT growth, whereas that of CNT- γ W samples increases with the concentration of ammonium tungstate aqueous solution. By excluding the weight of CNT growth catalyst, the loadings of WO₃ over the CNT-1W, CNT-5W, and CNT-10W are determined as around 7.0, 24.1, and 47.2 wt%, respectively. It can also be seen that the onset of carbon support decomposition shifts to low temperature with the loading of WO₃. This is most likely because the presence of WO₃ reduces the thermal stability of CNT in air by catalyzing the low-temperature oxidation of CNT, which has been also observed in previous studies (Chiang et al., 2001; Xin and Li, 2011).

Raman measurements were conducted to probe whether the incorporation of WO₃ affects the surface defects of CNT, for which the intensity ratio of D₁ band at \sim 1340 cm⁻¹ to G band at \sim 1570 cm⁻¹ (I_{D1}/I_G) is used to quantify the surface defects (Sadezky et al., 2005). As shown in Figure 1E, the I_{D1}/I_G values of CNT, CNT-1W, CNT-5W, and CNT-10W are 1.38, 1.37, 1.37, and 1.36, respectively, indicating neglectable influences of the WO₃ incorporation on the support surface defects. Low-magnification HAADF-STEM

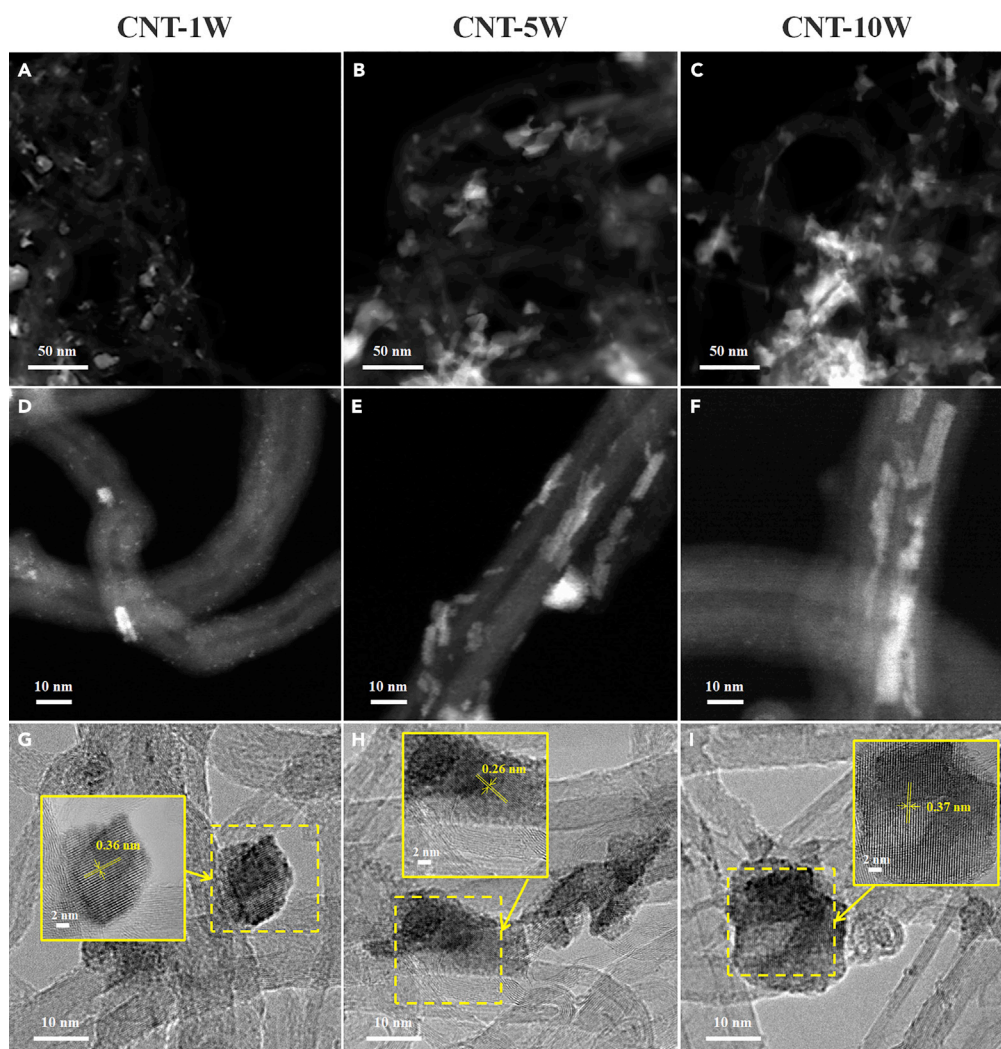


Figure 2. HAADF-STEM and HRTEM Images of CNT- γ W

(A–C) Low-magnification HAADF-STEM images of (A) CNT-1W, (B) CNT-5W, and (C) CNT-10W.

(D–F) High-magnification HAADF-STEM images of (D) CNT-1W, (E) CNT-5W, and (F) CNT-10W.

(G–I) HRTEM images of (G) CNT-1W, (H) CNT-5W, and (I) CNT-10W.

images of CNT- γ W in Figures 2A–2C show that the WO_3 appears as bright patches against the dark carbon matrix background. It can be seen that, for the CNT-1W with low WO_3 loading, the bright patches distribute homogeneously across the CNT surface in small sizes. With the increase of WO_3 loading, the density and size of these patches increase to high levels. In the high-magnification image of Figure 2D, some tiny WO_3 nanoparticles appear as bright dots on the CNT-1W, which could be due to the low tungsten loading as well as the strong interaction between WO_3 and CNT. In comparison, Figures 2E and 2F reveal that the CNT-5W and CNT-10W mainly consist of large strip-shaped particles along the CNT wall. Moreover, the HRTEM images in Figures 2G–2I exhibit continuous ordered lattice fringes, and the lattice spacings of ~ 0.36 and ~ 0.26 nm correspond to the (200) and (202) facets of WO_3 , respectively. These results are in good agreement with XRD results that the tungsten oxide species are mainly in the form of WO_3 , and the amount and size of WO_3 particles sharply increases with the WO_3 loading.

Synthesis and Structural Characterization of Pt- WO_3 Dual Sites

The above fabricated-tungsten-incorporated CNT- γ W samples as well as the pristine CNT as a reference were impregnated with H_2PtCl_6 solutions to prepare the catalysts, with an aim to construct Pt- WO_3 dual active sites. H_2 temperature-programmed reduction (H_2 -TPR) measurement was first conducted to explore

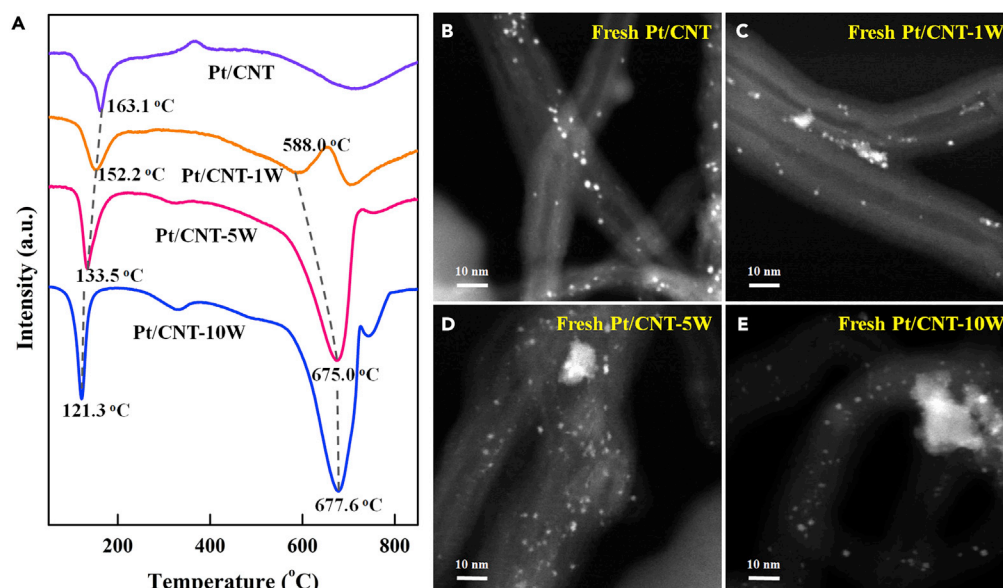


Figure 3. H₂-TPR Profiles and HAADF-STEM Images of Catalysts

(A) H₂-TPR profiles of Pt/CNT, Pt/CNT-1W, Pt/CNT-5W, and Pt/CNT-10W.

(B–E) Typical HAADF-STEM images of the fresh (B) Pt/CNT, (C) Pt/CNT-1W, (D) Pt/CNT-5W, and (E) Pt/CNT-10W catalysts.

the interactions among Pt, WO₃, and CNT. As shown in Figure 3A, for the pristine-CNT-supported Pt catalyst, two hydrogen consumption peaks could be observed at 163.1 and 709.3°C, which could be due to the reduction of platinum species and methanation of CNT support, respectively. However, for the Pt/CNT-γW catalysts, another new hydrogen consumption peak between the above two peaks is observed and ascribed to the reduction of WO₃. Notably, the increasing WO₃ loading leads to the upshift of WO₃ reduction peak, which eventually overlaps with the methanation peak, possibly due to the formation of larger WO₃ particles in Figures 1C and 2. Accordingly, the Pt species reduction peak shifts to low temperature with increasing WO₃ loading, resulting from the interaction of Pt with WO₃.

HAADF-STEM was employed to characterize the Pt particle size and distribution of these catalysts. Figure 3B reveals that the Pt particles on pristine CNT show a relatively homogeneous distribution, and the average Pt particle size based on the measurements of more than 200 random particles is determined to be 1.4 nm. In comparison, the Pt/CNT-1W in Figure 3C exhibits the coexistence of a few small patches, which could be WO₃ clusters, with some small spots, which could be Pt and WO₃ nanoparticles. Considering that the contrast variations in HAADF-STEM characterization are proportional to the square of the atomic number (Van Aert et al., 2011), the brighter and less bright spots could be ascribed to Pt and WO₃ nanoparticles, respectively. Therefore, it can be seen that a majority of Pt nanoparticles remain on the graphitic wall of CNT, whose sizes are similar to those of Pt/CNT, and a few bright Pt spots are observed on the WO₃ clusters.

As shown in Figures 3D and 3E, with the increase of WO₃ loading, the density of bright spots becomes intensive for Pt/CNT-5W and Pt/CNT-10W, making it difficult to distinguish Pt from WO₃ particles. Hence, energy dispersive spectroscopy (EDS) mapping of the selected areas in Figures 4A and 4B was further conducted to analyze the elemental distributions, and the results are shown in Figures 4C–4F. The EDS mapping of oxygen and tungsten in Figures 4D and 4E reveals that the Pt/CNT-5W mainly consists of large WO₃ patches as well as a few dispersed particles, consistent with the HAADF-STEM results. Interestingly, as shown in Figure 4F, the EDS mapping of Pt suggests that the Pt particles mainly concentrate on WO₃ patches instead of on CNT. Considering that the electron microscopic characterization could only reflect the local information of the sample, another two areas as depicted in Figures S2 and S3 were chosen by the same method to characterize this sample, so as to reduce the errors induced by the selected areas. Obviously, a majority of Pt particles still interact with WO₃ patches rather than with CNT, and the corresponding Pt particle sizes still remain in the range of 1–2 nm, which is comparable to that for the pristine CNT. Hence, all the above results indicate that the Pt particles prefer to interact with the WO₃ patches, which is consistent with the decreased reduction temperature as shown in Figure 3A.

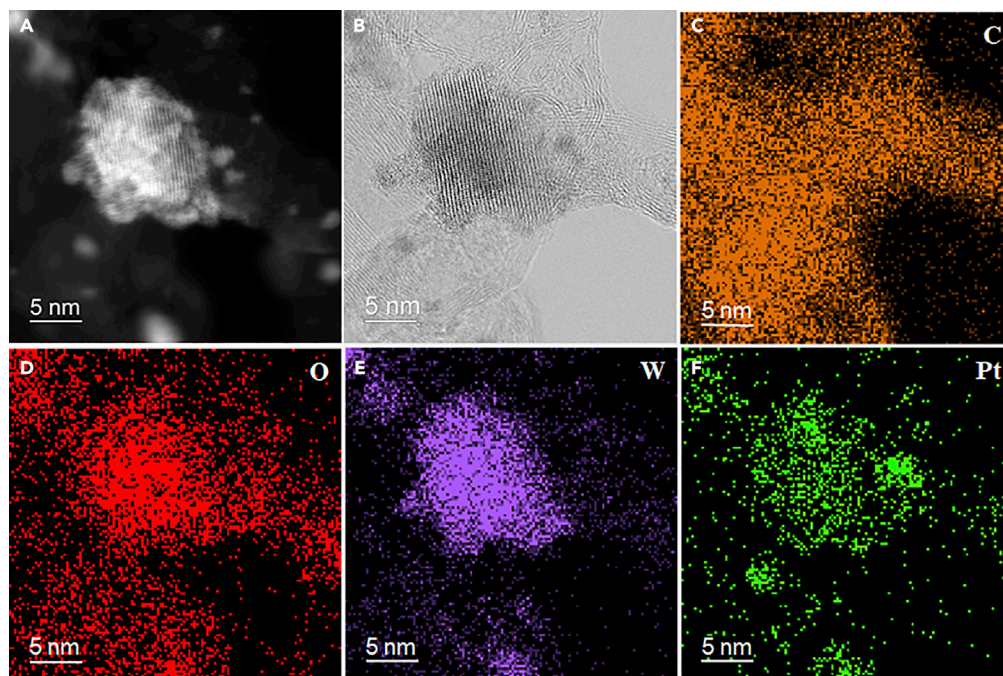


Figure 4. Atomic Distribution Characterization of Pt/CNT-5W Catalyst

(A) Typical HAADF-STEM image of Pt/CNT-5W.

(B) Typical HRTEM image of Pt/CNT-5W.

(C–F) The corresponding EDS mappings of (C) C, (D) O, (E) W, and (F) Pt elements.

XPS was employed to investigate the electronic properties of these catalysts, and the results are shown in Figure 5. The Pt 4f region of XPS spectra in Figure 5A shows two intense peaks corresponding to Pt 4f_{7/2} and Pt 4f_{5/2}, which can be deconvoluted into three pairs of doublets, i.e., Pt⁰, Pt²⁺, and Pt⁴⁺. Table S1 summarizes the binding energy (B.E.) as well as the corresponding percentage of Pt species. It can be seen that all the catalysts exhibit similar percentages of Pt⁰, which has been identified as the main active species for this reaction (Chandra and Xu, 2006). Interestingly, it is found that the Pt B.E. shifts to lower value with the WO₃ loading. Correspondingly, the deconvolution of W 4f region in Figure 5B shows an opposite trend of W B.E. Considering the similar Pt particle sizes for these catalysts, the observed Pt B.E. downshift and W B.E. upshift are mainly ascribed to electron transfer between Pt and WO₃. Specifically, WO₃ could act as an electron donor and transfer electrons to Pt, giving rise to the electron-rich Pt particles with lower Pt B.E. Hence, with the increase of Pt-WO₃ interactions, more and more electrons are transferred to Pt particles, resulting in the continuous decrease of Pt B.E. and increase of W B.E. for the Pt/CNT-γW catalysts.

Kinetic (Isotopic) and Durability Analyses

Catalytic behaviors of these Pt-WO₃ dual sites catalysts together with the reference Pt/CNT catalyst and CNT-5W were explored for ammonia borane hydrolysis, and the results are shown in Figures 6A and 6B. Obviously, the volume of hydrogen generation is proportional to the reaction time at the initial reaction stage (i.e., AB conversion lower than 45 ± 5%), suggesting pseudo-zero order kinetics for the reaction. As a result, the corresponding initial reaction rate (R_{initial}) can be calculated based on the slope of linear part for each plot in Figure 6A. As shown in Figure 6C, the R_{initial} values of Pt/CNT, Pt/CNT-1W, Pt/CNT-5W, and Pt/CNT-10W catalysts are determined as 165.2, 439.2, 710.1, and 557.5 mol_{H₂} · mol_{Pt}⁻¹ · min⁻¹, respectively. By combining previous results that the high Pt B.E. is favorable for ammonia borane hydrolysis (Chen et al., 2014, 2015), the Pt/CNT-γW catalysts with lower Pt B.E. than the Pt/CNT catalyst should give a lower hydrogen generation rate from the perspective of electronics, which is contradictory to the observation in Figure 6A. This strongly indicates that the fabrication of Pt-WO₃ dual sites is favorable for ammonia borane hydrolysis, verifying the above theoretical prediction of Pt-WO₃ acting as the dual active sites for this reaction.

To gain more insights into the reaction over such Pt-WO₃ dual active sites, kinetics analyses of Pt/CNT-γW against Pt/CNT were performed, and the results are shown in Figures S4 and 6C. Clearly, the Pt/CNT-γW

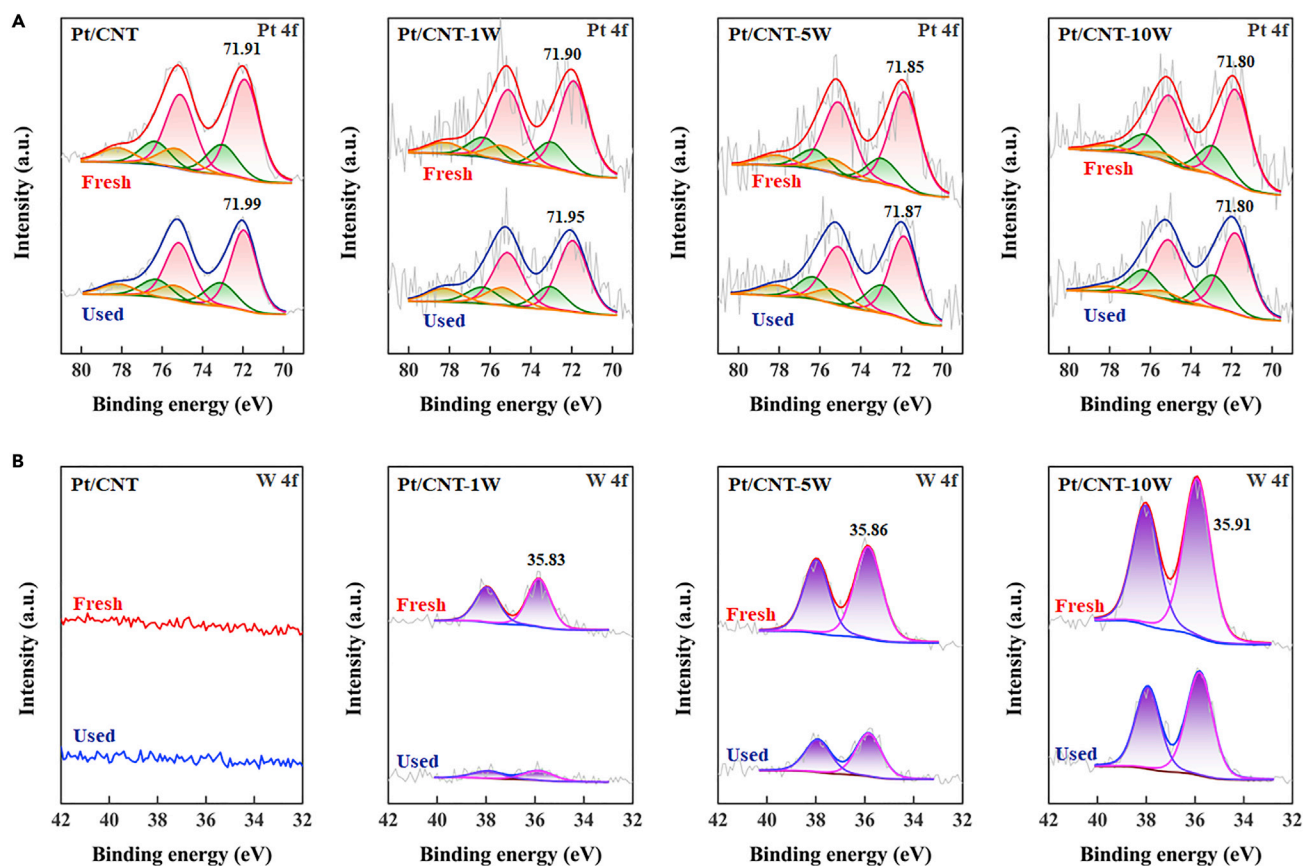


Figure 5. XPS Characterization of the Fresh and Used Catalysts

(A) Pt 4f spectra of the fresh and used catalysts.

(B) W 4f spectra of the fresh and used catalysts.

catalysts show lower activation energy (E_a) than the Pt/CNT catalyst, and the trend of E_a is consistent with that of R_{initial} mentioned above. This suggests that the fabrication of Pt- WO_3 dual active sites contributes to the enhanced kinetics. Furthermore, kinetic isotope experiments by replacing H_2O with D_2O as the reactant were conducted to probe the kinetic isotope effects and further the reaction mechanism (Chen et al., 2000), and the results are shown in Figures S5 and 6D. All the Pt/CNT- γ W catalysts exhibit the similar $k_{\text{H}}/k_{\text{D}}$ values (~ 2.6), which are higher than that of the Pt/CNT catalyst (1.9). The change in the $k_{\text{H}}/k_{\text{D}}$ is most likely ascribed to the change in the active sites, i.e., the single Pt site for the reaction over the Pt/CNT catalyst, but the dual Pt and WO_3 sites for the reaction over the Pt/CNT- γ W catalysts.

In addition, it was further explored whether the fabricated Pt/CNT- γ W catalysts could also improve the catalytic durability. Herein, the catalyst durability was investigated by adding an equivalent ammonia borane solution after the completion of last cycle. As shown in Figure S6, all the catalysts show decreased catalytic activity as a function of catalytic cycle with different extents. To make a clear comparison, the reaction rate in each cycle was normalized to that of the first cycle. It can be seen in Figures 6E and 6F that the incorporation of WO_3 remarkably promotes the catalytic durability of Pt/CNT, which increases with the WO_3 loading. The pH values of the reaction solutions were firstly measured in the range of 9.1–9.8 for all the catalysts during the reaction. This could be ascribed to the acid-base equilibrium of $\text{B}(\text{OH})_4^- \rightleftharpoons \text{B}(\text{OH})_3 + \text{OH}^-$ for the B-containing byproducts in the reaction solution (Chen et al., 2017a), considering that the $\text{p}K_a$ value of acid-base couple of $\text{B}(\text{OH})_3$ – $\text{B}(\text{OH})_4^-$ is 9.2 (Sanyal et al., 2011). Thus the similar pH values for the catalysts could help exclude their influences as the main reason for the significantly improved durability. To gain more insights, multiple characterizations were carried out to compare the catalyst properties before and after the durability test. HAADF-STEM measurements in Figures S7 and 3 indicate that some Pt agglomerations are observed after the durability test over Pt/CNT and Pt/CNT-1W, whereas no obvious agglomerations for Pt/CNT-5W and Pt/CNT-10W. This is most likely due to the strong interaction of Pt with WO_3 to

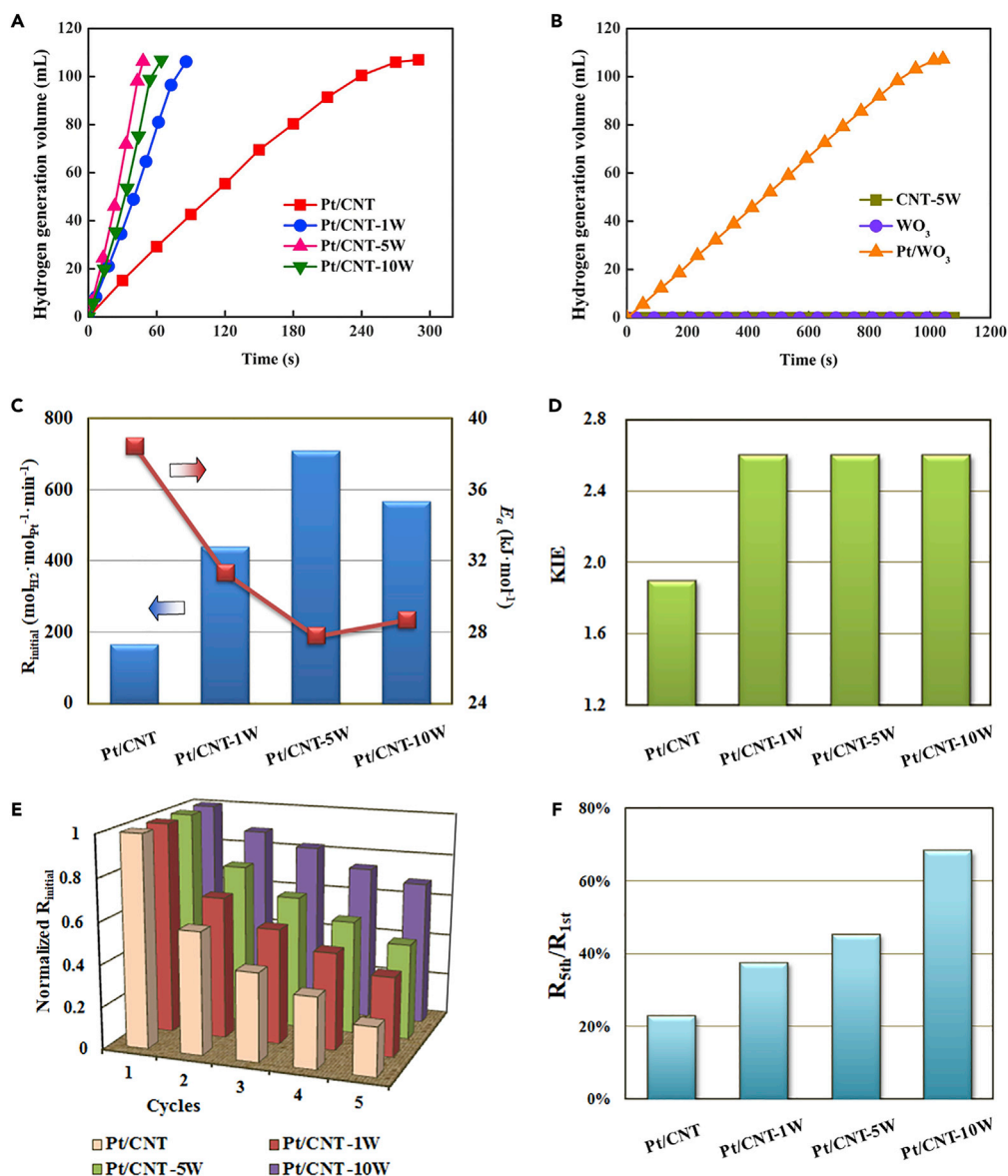


Figure 6. Catalytic Activity and Durability as well as Kinetics Analysis
 (A) Hydrogen generation as a function of time for Pt/CNT, Pt/CNT-1W, Pt/CNT-5W, and Pt/CNT-10W at 30°C.
 (B) Hydrogen generation as a function of time for CNT-5W, WO₃, and Pt/WO₃ at 30°C.
 (C) R_{initial} and E_a of Pt/CNT, Pt/CNT-1W, Pt/CNT-5W, Pt/CNT-10W, and CNT-5W.
 (D) Kinetic isotope effect (KIE) values of Pt/CNT, Pt/CNT-1W, Pt/CNT-5W, and Pt/CNT-10W.
 (E) The relative activities over cycles of Pt/CNT, Pt/CNT-1W, Pt/CNT-5W, and Pt/CNT-10W.
 (F) The ratio of the activity in the fifth cycle to that in the first run, $R_{5\text{th}}/R_{1\text{st}}$, for Pt/CNT, Pt/CNT-1W, Pt/CNT-5W, and Pt/CNT-10W.

suppress Pt agglomeration, being one factor for the higher catalyst durability of the Pt/CNT-5W and Pt/CNT-10W catalysts.

As mentioned above, the adsorption of B-containing by-products on the Pt surfaces is another main factor leading to the catalyst deactivation (Chen et al., 2014b). The XPS spectra in Figure 5A and their deconvolution results in Table S1 show that the used Pt catalysts exhibit positive shifts in Pt B.E. compared with the fresh ones, mainly ascribed to the electron-deficient nature of the adsorbed B-containing by-products (Chen et al., 2018). Considering that the change in XPS signal intensity is proportional to the concentration

of a given element per unit overlayer (Matrab et al., 2007; Precht et al., 2016), it has been previously used in our work (Chen et al., 2015) to compare the amount of species on the Pt surface. As shown in Figure 5, the used catalysts show slightly decreased XPS signal intensities for the Pt spectra but remarkably decreased ones for the W spectra in comparison with the fresh catalysts. This strongly suggests a preferential adsorption of B-containing by-products on the WO_3 surface during the reaction. In other words, WO_3 acts as the sacrificial site to preferentially adsorb B-containing by-products, which can suppress the adsorption of B-containing by-products on the Pt surfaces. Further combining the Pt/CNT-10W catalyst with the highest WO_3 loading, it would provide a rational interpretation for the Pt/CNT-10W catalyst with the highest durability, i.e., retaining 68% of its initial activity at the fifth cycle ($R_{5\text{th}}/R_{1\text{st}}$) in comparison with 24% for the Pt/CNT catalyst, which mainly arises from the most sacrificial sites of WO_3 for the adsorption of B-containing by-products.

Mechanism of Pt- WO_3 Dual Sites for Enhanced Activity and Durability

As described above, DFT calculations show that the activation of ammonia borane reactant proceeds by its dissociative adsorption on the Pt site, and the WO_3 site exhibits much lower activation barrier for H_2O dissociation than on the Pt site. On a single Pt active site, ammonia borane hydrolysis over the Pt/CNT catalyst has been demonstrated to proceed by the NH_3BH_2^* -assisted cleavage of O-H bond within H_2O (Chen et al., 2017a). Interestingly, on the Pt- WO_3 dual active sites, the kinetics (isotope) analysis shows significantly decreased activation energy of the reaction, but an increase in $k_{\text{H}}/k_{\text{D}}$ ratio from 1.9 to 2.6, which contribute to the enhanced kinetics for the reaction over the Pt/CNT- γ W catalysts.

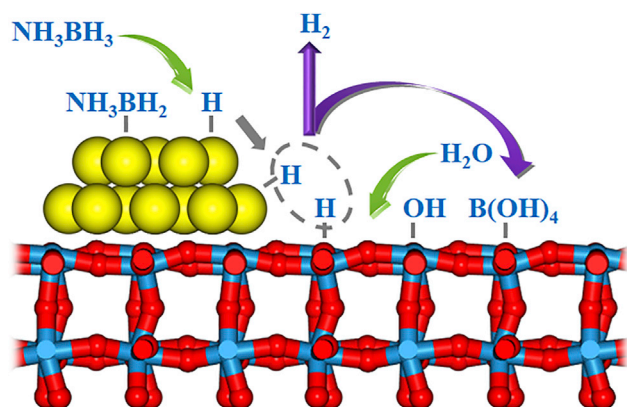
The strategy demonstrated above has been successfully developed to fabricate high specific surface area of WO_3 by incorporating it onto the CNT with larger specific surface area, close ends, and mesoporous structure, which is a promising candidate to immobilize Pt for favorably constructing Pt- WO_3 dual active sites and enhancing hydrogen generation activity. If directly using commercial WO_3 (usually having relatively low specific surface area) as the catalyst or catalyst support, the catalyst testing results in Figure 6B show that the WO_3 is almost inactive for the reaction, and the Pt/ WO_3 catalyst gives much lower hydrogen generation rate than the Pt/CNT- γ W catalysts, mainly due to the larger Pt particle size and undesirable Pt B.E. in Figure S8. Therefore, the fabrication of Pt- WO_3 immobilized on the CNT is suggested as an effective way to obtain more Pt- WO_3 dual active sites for the promoted reaction.

In our previous studies (Chen et al., 2014, 2017), it has been found that the electron-deficient Pt particles with the higher Pt B.E. facilitates the adsorption and activation of the reactants toward fast hydrogen evolution. In the present study, the incorporation of WO_3 not only leads to the Pt/CNT- γ W catalysts with lower Pt B.E. than the Pt/CNT catalyst, unfavorable for the reaction, but also fabricates highly active Pt- WO_3 dual active sites, favorable for the reaction. Such trade-off between the promotion effects of WO_3 and the negative electronic effects of Pt B.E. can pave an explanation for the observed volcano-shaped activity in Figure 6C.

In addition, the incorporation of WO_3 also demonstrates remarkable enhancements in the durability. This is attributed to the preferential adsorption of B-containing by-products over the WO_3 sites. As the reaction proceeds, the produced B-containing by-products would transfer and accumulate on the WO_3 site instead of the Pt site. Considering that WO_3 is in large excess, the accumulation of B-containing by-products has much less influence on the activity. Therefore, the WO_3 site is also suggested as the sacrificial site, diverting B-containing by-products away from the Pt site during the reaction. With the increase of WO_3 loading, more and more Pt sites in contact with WO_3 sites are sterically protected from deactivation.

Based on the discussion of the mechanism of Pt- WO_3 dual sites for the enhanced activity and durability, Scheme 1 is proposed to mainly illustrate ammonia borane hydrolysis over Pt- WO_3 dual active sites, in which the Pt site and WO_3 site contribute to the activation of ammonia borane and H_2O , respectively. On the other hand, the WO_3 site also acts as the sacrificial site to preferentially adsorb B-containing by-products, which can suppress the adsorption of B-containing by-products on the Pt surfaces. Such cooperativity between Pt and WO_3 sites creates a unique synergy and demonstrates robust hydrogen generation from ammonia borane hydrolysis.

In addition, Table 1 gives a comparison of the activity and durability of Pt/CNT-W catalysts developed in this study with various monometallic Pt-based catalysts in the literature. Obviously, the Pt/CNT-W catalysts



Scheme 1. A Proposed Mechanism for Ammonia Borane Hydrolysis over Pt-WO₃ Dual Metal Sites

show a superior hydrogen generation activity in addition to relatively high durability. Our previous studies have identified Pt(111) as the dominant active sites for the reaction, whose number reaches the optimal value at the mean Pt particle size of ~ 1.8 nm (Chen et al., 2014b); and the high Pt B.E. is favorable for both the hydrogen generation activity and durability (Chen et al., 2014a). Thus, the fabricated Pt-WO₃ dual sites enhance not only the hydrogen generation activity and kinetics due to the Pt-WO₃ dual active sites but also the durability due to the sacrificial site of WO₃ for the preferential adsorption of B-containing byproducts during the reaction. Moreover, it can be seen in Table 1 that the employment of carbon support plays a crucial role in Pt electronic properties to remarkably increase the catalytic activity, and the dual sites of Pt-metal oxides (MO, e.g., CeO₂, Fe₃O₄ and TiO₂) endow the catalysts with a significantly enhanced durability. All of these discussions could shed a new light on the rational design and manipulation of highly active and durable Pt-based catalysts for the reaction, e.g., fabricating Pt-MO/C multifunctional catalysts with appropriate transition metal and carbon toward significantly enhanced hydrogen generation activity and durability.

DISCUSSION

In summary, we report for the first time the fabrication and manipulation of multifunctional Pt-WO₃/CNT catalysts with simultaneously enhanced hydrogen generation activity and durability. A combination of DFT calculations and multiple characterizations with kinetic (isotopic) analysis demonstrates that the Pt-WO₃ acts as the dual active sites for the activation of ammonia borane and H₂O. By incorporating the WO₃ onto CNT to immobilize Pt particles, the resultant Pt/CNT- γ W catalysts give rise to more Pt-WO₃ dual active sites with the desirable Pt B.E. than the commercial WO₃-supported Pt catalyst. By increasing WO₃ loading, a trade-off between the promotion effect of WO₃ and the negative electronic effect of decreased Pt binding energy contributes the volcano-shaped activity, in which the Pt/CNT-5W delivers the highest catalytic activity of $710.1 \text{ mol}_{\text{H}_2} \cdot \text{mol}_{\text{Pt}}^{-1} \cdot \text{min}^{-1}$, more than four folds higher than that of pristine Pt/CNT. On the other hand, the WO₃ site acts as the sacrificial site and diverts B-containing by-products away from the Pt site, thus inhibiting the catalyst deactivation during the reaction and yielding a significant increase from 24% to 68% of the initial catalytic activity after five cycles. This report not only shows a high potential to achieve robust hydrogen generation from ammonia borane hydrolysis but also guides the rational design and manipulation of dual-site catalysts with the multifunctional properties by combining theoretical and experimental studies.

Limitations of the Study

Currently, it is very difficult for this research to precisely characterize the microstructures of the fabricated highly active and durable Pt/CNT- γ W catalysts at an atomic level. This would be facilitated by advanced in-situ/ex-situ catalyst characterization, such as Cs-corrected TEM and XAS. Then, more desirable theoretical models are needed for in-depth understanding of the reaction mechanism and kinetics to reveal the underlying dual-active-site mechanism.

METHODS

All methods can be found in the accompanying [Transparent Methods supplemental file](#).

Catalyst	d _{Pt} (nm)	Pt B.E. (eV)	R (mol _{H₂} ·mol _M ⁻¹ ·min ⁻¹)	E _a (kJ·mol ⁻¹)	Durability	Ref.
Commercial Pt/C	2.5	–	83.3 ^{a,b}	–	–	Chandra and Xu, 2007
Pt/C	1.9	–	111 ^{a,b}	–	–	Chandra and Xu, 2007
Pt(8%)/CCF-500	3.4	71.80	35 ^c	39.2	47% (r _{5th} /r _{1st}) ^a	Yuan et al., 2017
(Zn ¹⁺)Pt/RGO	1.2	~71.5	284 ^b	–	49% (r _{5th} /r _{1st}) ^a	Chen et al., 2017c
SiO ₂ @Pt@NGO	1.9	71.12	324.6 ^c	–	39% (r _{6th} /r _{1st})	Ye et al., 2017
Pt20/CNT	1.9	71.5	416.5 ^b	48.3	40% (r _{4th} /r _{1st})	Zhang et al., 2017
Pt/CNT-G	2.8	–	135 ^b	35.3	–	Uzundurukan and Devrim, 2019
Pt/CNT-P	1.4	71.9	141.7 ^c	–	24% (r _{5th} /r _{1st})	Chen et al., 2015
Pt/CNT-O	1.6	71.7	54.4 ^c	–	~43% (r _{5th} /r _{1st})	Chen et al., 2015
Pt/CNT-D	1.3	72.0	416.0 ^c	–	~62% (r _{5th} /r _{1st})	Chen et al., 2015
Pt/CNT-5W	~1.4	71.85	710 ^c	27.8	45% (r _{5th} /r _{1st})	This work
Pt/CNT-10W	~1.4	71.80	558 ^c	28.7	68% (r _{5th} /r _{1st})	This work
Pt-CeO ₂ /rGO	2.8	71.26	93.8 ^b	64.7	92% (r _{10th} /r _{1st})	Yao et al., 2016
Pt/SiO ₂	5.1	–	55 ^a	–	–	Chandra and Xu, 2007
Pt@MIL-101	1.8	–	414 ^b	–	–	Aijaz et al., 2012
Fe ₃ O ₄ @SiO ₂ @Pt@mSiO ₂	–	–	5.5 ^d	35.4	62% (r _{5th} /r _{1st}) ^a	Xu et al., 2017
Pt-CeO ₂	5.0	–	133 ^b	–	66% (r _{5th} /r _{1st})	Wang et al., 2012
SEA-Pt/HNTs	1.5	–	321 ^b	49.2	71% (r _{10th} /r _{1st})	Yin et al., 2019
Pt25@TiO ₂	2.4	71.02	311 ^b	–	75% (r _{3rd} /r _{1st})	Khalily et al., 2016

Table 1. A Comparison of the Activity and Durability over Monometallic Pt-Based Catalysts for Ammonia Borane Hydrolysis

^aEstimated from the slope of the fitting line.

^bMeasured under 25°C.

^cMeasured under 30°C.

^dMeasured under 35°C.

SUPPLEMENTAL INFORMATION

Supplemental Information can be found online at <https://doi.org/10.1016/j.isci.2020.100922>.

ACKNOWLEDGMENTS

This work was financially supported by the Natural Science Foundation of China (21922803 and 21776077), the Shanghai Natural Science Foundation (17ZR1407300 and 17ZR1407500), the China Postdoctoral Science Foundation (BX20190116), the Program for Professor of Special Appointment (Eastern Scholar) at Shanghai Institutions of Higher Learning, the Shanghai Rising-Star Program (17QA1401200), the State Key Laboratory of Organic-Inorganic Composites (oic-201801007), and the Open Project of State Key Laboratory of Chemical Engineering (SKLChE-15C03).

AUTHOR CONTRIBUTIONS

W.C. performed the catalysts preparation and characterization, catalytic measurements, and wrote the manuscript. W.F. and G.Q. contributed to theoretical calculations. B.Z. contributed to the HAADF-STEM characterization. D.C. and X.Z. helped to analyze the data and modify the paper. X.D. conceived the idea, analyzed the data, and wrote the paper. All authors contributed to the preparation of the manuscript.

DECLARATION OF INTERESTS

The authors declare no competing interests.

Received: November 17, 2019

Revised: February 6, 2020

Accepted: February 13, 2020

Published: March 27, 2020

REFERENCES

- Aijaz, A., Karkamkar, A., Choi, Y.J., Tsumori, N., Ronnebro, E., Autrey, T., Shioyama, H., and Xu, Q. (2012). Immobilizing highly catalytically active Pt nanoparticles inside the pores of metal-organic framework: a double solvents approach. *J. Am. Chem. Soc.* *134*, 13926–13929.
- Akbayrak, S., and Ozkar, S. (2012). Ruthenium (0) nanoparticles supported on multiwalled carbon nanotube as highly active catalyst for hydrogen generation from ammonia-borane. *ACS Appl. Mater. Interfaces* *4*, 6302–6310.
- Allian, A.D., Takanabe, K., Fajdala, K.L., Hao, X., Truex, T.J., Cai, J., Buda, C., Neurock, M., and Iglesia, E. (2011). Chemisorption of CO and mechanism of CO oxidation on supported platinum nanoclusters. *J. Am. Chem. Soc.* *133*, 4498–4517.
- Aramouni, N.A.K., Touma, J.G., Tarboush, B.A., Zeaiter, J., and Ahmad, M.N. (2018). Catalyst design for dry reforming of methane: analysis review. *Renew. Sustain. Energ. Rev.* *82*, 2570–2585.
- Cao, A.M., Lu, R.W., and Veser, G. (2010). Stabilizing metal nanoparticles for heterogeneous catalysis. *Phys. Chem. Chem. Phys.* *12*, 13499–13510.
- Chandra, M., and Xu, Q. (2006). A high-performance hydrogen generation system: transition metal-catalyzed dissociation and hydrolysis of ammonia-borane. *J. Power Sources* *156*, 190–194.
- Chandra, M., and Xu, Q. (2007). Room temperature hydrogen generation from aqueous ammonia-borane using noble metal nanoclusters as highly active catalysts. *J. Power Sources* *168*, 135–142.
- Chen, K., Iglesia, E., and Bell, A.T. (2000). Kinetic isotopic effects in oxidative dehydrogenation of propane on vanadium oxide catalysts. *J. Catal.* *192*, 197–203.
- Chen, W., Ji, J., Duan, X., Qian, G., Li, P., Zhou, X., Chen, D., and Yuan, W. (2014a). Unique reactivity in Pt/CNT catalyzed hydrolytic dehydrogenation of ammonia borane. *Chem. Commun. (Camb.)* *50*, 2142–2144.
- Chen, W., Ji, J., Feng, X., Duan, X., Qian, G., Li, P., Zhou, X., Chen, D., and Yuan, W. (2014b). Mechanistic insight into size-dependent activity and durability in Pt/CNT catalyzed hydrolytic dehydrogenation of ammonia borane. *J. Am. Chem. Soc.* *136*, 16736–16739.
- Chen, W., Duan, X., Qian, G., Chen, D., and Zhou, X. (2015). Carbon nanotubes as support in the platinum-catalyzed hydrolytic dehydrogenation of ammonia borane. *ChemSusChem* *8*, 2927–2931.
- Chen, W., Li, D., Wang, Z., Qian, G., Sui, Z., Duan, X., Zhou, X., Yeboah, I., and Chen, D. (2017a). Reaction mechanism and kinetics for hydrolytic dehydrogenation of ammonia borane on a Pt/CNT Catalyst. *AIChE J.* *63*, 60–65.
- Chen, W., Li, D., Peng, C., Qian, G., Duan, X., Chen, D., and Zhou, X. (2017b). Mechanistic and kinetic insights into the Pt-Ru synergy during hydrogen generation from ammonia borane over PtRu/CNT nanocatalysts. *J. Catal.* *356*, 186–196.
- Chen, Y., Yang, X., Kitta, M., and Xu, Q. (2017c). Monodispersed Pt nanoparticles on reduced graphene oxide by a non-noble metal sacrificial approach for hydrolytic dehydrogenation of ammonia borane. *Nano Res.* *10*, 3811–3816.
- Chen, W., Wang, Z., Duan, X., Qian, G., Chen, D., and Zhou, X. (2018). Structural and kinetic insights into Pt/CNT catalysts during hydrogen generation from ammonia borane. *Chem. Eng. Sci.* *192*, 1242–1251.
- Chiang, I.W., Brinson, B.E., Smalley, R.E., Margrave, J.L., and Hauge, R.H. (2001). Purification and characterization of single-wall carbon nanotubes. *J. Phys. Chem. B* *105*, 1157–1161.
- Chin, Y.H., Buda, C., Neurock, M., and Iglesia, E. (2011). Reactivity of chemisorbed oxygen atoms and their catalytic consequences during CH₄-O₂ catalysis on supported Pt clusters. *J. Am. Chem. Soc.* *133*, 15958–15978.
- Dasgupta, N.P., Liu, C., Andrews, S., Prinz, F.B., and Yang, P. (2013). Atomic layer deposition of platinum catalysts on nanowire surfaces for photoelectrochemical water reduction. *J. Am. Chem. Soc.* *135*, 12932–12935.
- Demirkan, B., Kuyuldar, E., Karatas, Y., Gulcan, M., and Sen, F. (2019). Ex situ synthesis and characterization of a polymer-carbon nanotube-based hybrid nanocatalyst with one of the highest catalytic activities and stabilities for the hydrolytic dehydrogenation of hydrazine-borane at room temperature conditions. *J. Colloid Interface Sci.* *552*, 432–438.
- Diakov, V., Diwan, M., Shafirovich, E., and Varma, A. (2007). Mechanistic studies of combustion-stimulated hydrogen generation from sodium borohydride. *Chem. Eng. Sci.* *62*, 5586–5591.
- Diwan, M., Hwang, H.T., Al-Kukhun, A., and Varma, A. (2011). Hydrogen generation from noncatalytic hydrothermolysis of ammonia borane for vehicle applications. *AIChE J.* *57*, 259–264.
- Gong, F., Wang, H., Xu, X., Zhou, G., and Wang, Z.S. (2012). In situ growth of Co_{0.85}Se and Ni_{0.85}Se on conductive substrates as high-performance counter electrodes for dye-sensitized solar cells. *J. Am. Chem. Soc.* *134*, 10953–10958.
- Hmadeh, M., Hoepfner, V., Larios, E., Liao, K., Jia, J., Jose-Yacaman, M., and Ozin, G.A. (2014). New hydrogen-evolution heteronanostructured photocatalysts: Pt-Nb₃O₇(OH) and Cu-Nb₃O₇(OH). *ChemSusChem* *7*, 2104–2109.
- Hurtado-Aular, O., Vidal, A.B., Sierraalta, A., and Anez, R. (2020). Periodic DFT study of water adsorption on m-WO₃ (001), m-WO₃ (100), h-WO₃ (001) and h-WO₃ (100). Role of hydroxyl groups on the stability of polar hexagonal surfaces. *Surf. Sci.* *694*, 121558.
- Ishikawa, Y., Liao, M.S., and Cabrera, C.R. (2002). Energetics of H₂O dissociation and CO_{ads}+OH_{ads} reaction on a series of Pt-M mixed metal clusters: a relativistic density-functional study. *Surf. Sci.* *513*, 98–110.
- Jin, Y.X., Han, D.M., Jia, W.P., Li, F., Chen, X.Y., Huang, G.B., and Zhang, D. (2017). WO₃ modified graphene supported Pt electrocatalysts with enhanced performance for oxygen reduction reaction. *Int. J. Electrochem. Sci.* *12*, 6535–6544.
- Khalily, M.A., Eren, H., Akbayrak, S., Susapto, H.H., Biyikli, N., Ozkar, S., and Guler, M.O. (2016). Facile synthesis of three-dimensional Pt-TiO₂ Nano-networks: a highly active catalyst for the hydrolytic dehydrogenation of ammonia-borane. *Angew. Chem. Int. Ed.* *55*, 12257–12261.
- Lara, P., Philippot, K., and Suarez, A. (2019). Phosphane-decorated platinum nanoparticles as efficient catalysts for H₂ generation from ammonia borane and methanol. *ChemCatChem* *11*, 766–771.
- Li, Z., He, T., Liu, L., Chen, W., Zhang, M., Wu, G., and Chen, P. (2017). Covalent triazine framework supported non-noble metal nanoparticles with superior activity for catalytic hydrolysis of ammonia borane: from mechanistic study to catalyst design. *Chem. Sci.* *8*, 781–788.
- Mahata, A., and Pathak, B. (2017). Bimetallic core-based cuboctahedral core-shell nanoclusters for the formation of hydrogen peroxide (2e⁻ reduction) over water (4e⁻ reduction): role of core metals. *Nanoscale* *9*, 9537–9547.
- Matrab, T., Save, M., Charleux, B., Pinson, J., Cabet-Deliry, E., Adenier, A., Chehimi, M.M., and Delamar, M. (2007). Grafting densely-packed poly (n-butyl methacrylate) chains from an iron substrate by aryl diazonium surface-initiated ATRP: XPS monitoring. *Surf. Sci.* *601*, 2357–2366.

- Meirer, F., and Weckhuysen, B.M. (2018). Spatial and temporal exploration of heterogeneous catalysts with synchrotron radiation. *Nat. Rev. Mater.* 3, 324–340.
- Metin, O., Mazumder, V., Ozkar, S., and Sun, S. (2010). Monodisperse nickel nanoparticles and their catalysis in hydrolytic dehydrogenation of ammonia borane. *J. Am. Chem. Soc.* 132, 1468–1469.
- Mori, K., Miyawaki, K., and Yamashita, H. (2016). Ru and Ru-Ni nanoparticles on TiO₂ support as extremely active catalysts for hydrogen production from ammonia-borane. *ACS Catal.* 6, 3128–3135.
- Moussa, G., Moury, R., Demirci, U.B., Sener, T., and Miele, P. (2013). Boron-based hydrides for chemical hydrogen storage. *Int. J. Energy Res.* 37, 825–842.
- Norskov, J.K., Abild-Pedersen, F., Studt, F., and Bligaard, T. (2011). Density functional theory in surface chemistry and catalysis. *Proc. Natl. Acad. Sci. U S A* 108, 937–943.
- Pakhare, D., and Spivey, J. (2014). A review of dry (CO₂) reforming of methane over noble metal catalysts. *Chem. Soc. Rev.* 43, 7813–7837.
- Pan, X., and Bao, X. (2011). The effects of confinement inside carbon nanotubes on catalysis. *Acc. Chem. Res.* 44, 553–562.
- Precht, R., Stolz, S., Mankel, E., Mayer, T., Jaegermann, W., and Hausbrand, R. (2016). Investigation of sodium insertion into tetracyanoquinodimethane (TCNQ): results for a TCNQ thin film obtained by a surface science approach. *Phys. Chem. Chem. Phys.* 18, 3056–3064.
- Qiao, B., Wang, A., Yang, X., Allard, L.F., Jiang, Z., Cui, Y., Liu, J.Y., Li, J., and Zhang, T. (2011). Single-atom catalysis of CO oxidation using Pt₁/FeO_x. *Nat. Chem.* 3, 634–641.
- Sadezky, A., Muckenhuber, H., Grothe, H., Niessner, R., and Poschl, U. (2005). Raman microspectroscopy of soot and related carbonaceous materials: spectral analysis and structural information. *Carbon* 43, 1731–1742.
- Sanyal, U., Demirci, U.B., Jagirdar, B.R., and Miele, P. (2011). Hydrolysis of ammonia borane as a hydrogen source: fundamental issues and potential solutions towards implementation. *ChemSusChem* 4, 1731–1739.
- Sen, B., Demirkan, B., Levent, M., Savk, A., and Sen, F. (2018). Silica-based monodisperse PdCo nanohybrids as highly efficient and stable nanocatalyst for hydrogen evolution reaction. *Int. J. Hydrogen Energy* 43, 20234–20242.
- Sogut, E.G., Acidereli, H., Kuyuldar, E., Karatas, Y., Gulcan, M., and Sen, F. (2019). Single-walled carbon nanotube supported Pt-Ru bimetallic superb nanocatalyst for the hydrogen generation from the methanolysis of methylamine-borane at mild conditions. *Sci. Rep.* 9, 1–9.
- Shrestha, S., Liu, Y., and Mustain, W.E. (2011). Electrocatalytic activity and stability of Pt clusters on state-of-the-art supports: a review. *Catal. Rev.* 53, 256–336.
- Sverjensky, D.A., and Fukushi, K. (2006). Anion adsorption on oxide surfaces: inclusion of the water dipole in modeling the electrostatics of ligand exchange. *Environ. Sci. Technol.* 40, 263–271.
- Turner, J.A. (2004). Sustainable hydrogen production. *Science* 305, 972–974.
- Uzundurukan, A., and Devrim, Y. (2019). Carbon nanotube-graphene hybrid supported platinum as an effective catalyst for hydrogen generation from hydrolysis of ammonia borane. *Int. J. Hydrogen Energy* 44, 26773–26782.
- Valero-Pedraza, M.J., Cot, D., Petit, E., Aguey-Zinsou, K.F., Alauzun, J.G., and Demirci, U.B. (2019). Ammonia borane nanospheres for hydrogen storage. *ACS Appl. Nano Mater.* 2, 1129–1138.
- Van Aert, S., Batenburg, K.J., Rossell, M.D., Erni, R., and Van Tendeloo, G. (2011). Three-dimensional atomic imaging of crystalline nanoparticles. *Nature* 470, 374–377.
- Wang, X., Liu, D., Song, S., and Zhang, H. (2012). Synthesis of highly active Pt-CeO₂ hybrids with tunable secondary nanostructures for the catalytic hydrolysis of ammonia borane. *Chem. Commun. (Camb.)* 48, 10207–10209.
- Wang, S., Zhang, D., Ma, Y., Zhang, H., Gao, J., Nie, Y., and Sun, X. (2014). Aqueous solution synthesis of Pt-M (M = Fe, Co, Ni) bimetallic nanoparticles and their catalysis for the hydrolytic dehydrogenation of ammonia borane. *ACS Appl. Mater. Interfaces* 6, 12429–12435.
- Wu, G., More, K.L., Johnston, C.M., and Zelenay, P. (2011). High-performance electrocatalysts for oxygen reduction derived from polyaniline, iron, and cobalt. *Science* 332, 443–447.
- Wu, Y., Cai, S., Wang, D., He, W., and Li, Y. (2012). Syntheses of water-soluble octahedral, truncated octahedral, and cubic Pt-Ni nanocrystals and their structure-activity study in model hydrogenation reactions. *J. Am. Chem. Soc.* 134, 8975–8981.
- Xin, F., and Li, L. (2011). Decoration of carbon nanotubes with silver nanoparticles for advanced CNT/polymer nanocomposites. *Compos. Part A Appl. Sci. Manuf.* 42, 961–967.
- Xu, D., Cui, Z., Yang, J., Yuan, M., Cui, X., Zhang, X., and Dong, Z. (2017). Pt nanoparticles immobilized in mesoporous silica-coated magnetic nanocapsules: a non-leaching catalyst for hydrogen generation from hydrolysis of ammonia borane. *Int. J. Hydrogen Energy* 42, 27034–27042.
- Yamada, Y., Tsung, C.K., Huang, W., Huo, Z., Habas, S.E., Soejima, T., Aliaga, C.E., Somorjai, G.A., and Yang, P. (2011). Nanocrystal bilayer for tandem catalysis. *Nat. Chem.* 3, 372–376.
- Yan, J.M., Zhang, X.B., Han, S., Shioyama, H., and Xu, Q. (2008). Iron-nanoparticle-catalyzed hydrolytic dehydrogenation of ammonia borane for chemical hydrogen storage. *Angew. Chem. Int. Ed.* 47, 2287–2289.
- Yan, H., Lin, Y., Wu, H., Zhang, W., Sun, Z., Cheng, H., Liu, W., Wang, C.L., Li, J.J., Huang, X.H., et al. (2017). Bottom-up precise synthesis of stable platinum dimers on graphene. *Nat. Commun.* 8, 1070.
- Yang, X., Cheng, F., Tao, Z., and Chen, J. (2011). Hydrolytic dehydrogenation of ammonia borane catalyzed by carbon supported Co core-Pt shell nanoparticles. *J. Power Sources* 196, 2785–2789.
- Yang, Y., Niu, S., Han, D., Liu, T., Wang, G., and Li, Y. (2017). Progress in developing metal oxide nanomaterials for photoelectrochemical water splitting. *Adv. Energy Mater.* 7, 1700555.
- Yao, Q., Shi, Y., Zhang, X., Chen, X., and Lu, Z.H. (2016). Facile synthesis of platinum-cerium (IV) oxide hybrids arched on reduced graphene oxide catalyst in reverse micelles with high activity and durability for hydrolysis of ammonia borane. *Chem. Asian J.* 11, 3251–3257.
- Ye, W., Ge, Y., Gao, Z., Lu, R., and Zhang, S. (2017). Enhanced catalytic activity and stability of Pt nanoparticles by surface coating of nanosized graphene oxide for hydrogen production from hydrolysis of ammonia-borane. *Sustain. Energy Fuels* 1, 2128–2133.
- Yin, L., Feng, Y., Zhou, X., Dai, K., Gao, X., Zhao, Y., and Zhang, B. (2019). Synthesis of Pt nanocatalyst supported on halloysite nanotubes via strong electronic adsorption for hydrolytic dehydrogenation of ammonia borane. *Chem. Lett.* 48, 1084–1087.
- Yu, W., Porosoff, M.D., and Chen, J.G. (2012). Review of Pt-based bimetallic catalysis: from model surfaces to supported catalysts. *Chem. Rev.* 112, 5780–5817.
- Yuan, M., Cui, Z., Yang, J., Cui, X., Tian, M., Xu, D., Ma, J., and Dong, Z. (2017). Ultrafine platinum nanoparticles modified on cotton derived carbon fibers as a highly efficient catalyst for hydrogen evolution from ammonia borane. *Int. J. Hydrogen Energy* 42, 29244–29253.
- Zecevic, J., van der Eerden, A.M., Friedrich, H., de Jong, P.E., and de Jong, K.P. (2013). Heterogeneities of the nanostructure of platinum/zeolite Y catalysts revealed by electron tomography. *ACS Nano* 7, 3698–3705.
- Zhang, X.B., Yan, J.M., Han, S., Shioyama, H., and Xu, Q. (2009). Magnetically recyclable Fe@Pt core-shell nanoparticles and their use as electrocatalysts for ammonia borane oxidation: the role of crystallinity of the core. *J. Am. Chem. Soc.* 131, 2778–2779.
- Zhang, J., Chen, C., Chen, S., Hu, Q., Gao, Z., Li, Y., and Qin, Y. (2017). Highly dispersed Pt nanoparticles supported on carbon nanotubes produced by atomic layer deposition for hydrogen generation from hydrolysis of ammonia borane. *Catal. Sci. Technol.* 7, 322–329.
- Zhang, J., Chen, W., Ge, H., Chen, C., Yan, W., Gao, Z., Gan, J., Zhang, B.Y., Duan, X.Z., and Qin, Y. (2018). Synergistic effects in atomic-layer-deposited PtCo_x/CNTs catalysts enhancing hydrolytic dehydrogenation of ammonia borane. *Appl. Catal. B Environ.* 235, 256–263.
- Zhou, Y., Neyerlin, K., Olson, T.S., Pylpenko, S., Bult, J., Dinh, H.N., Gennett, T., Shao, Z.P., and O'Hayre, R. (2010). Enhancement of Pt and Pt-alloy fuel cell catalyst activity and durability via nitrogen-modified carbon supports. *Environ. Sci.* 3, 1437–1446.

iScience, Volume 23

Supplemental Information

Synergistic Pt-WO₃ Dual Active Sites to Boost Hydrogen Production from Ammonia Borane

Wenyao Chen, Wenzhao Fu, Gang Qian, Bingsen Zhang, De Chen, Xuezhi Duan, and Xingui Zhou

Supporting Information

Supplemental Table

Table S1. The binding energy (B.E.) as well as corresponding percentage of Pt species determined by XPS for the fresh and used catalysts, related to Figure 5.

Catalyst		Pt ⁿ 4f _{7/2} B.E. (eV)			Pt ⁿ percentage		
		Pt ⁰	Pt ²⁺	Pt ⁴⁺	Pt ⁰	Pt ²⁺	Pt ⁴⁺
Pt/CNT	Fresh	71.91	73.00	75.30	64.4%	20.7%	14.9%
	Used	71.99	73.03	75.31	63.4%	21.6%	15.0%
Pt/CNT-1W	Fresh	71.90	73.00	75.30	67.7%	19.2%	13.1%
	Used	71.95	73.05	75.35	61.9%	20.2%	17.9%
Pt/CNT-5W	Fresh	71.85	72.95	75.26	69.7%	18.6%	11.7%
	Used	71.87	72.95	75.30	62.6%	24.0%	13.4%
Pt/CNT-10W	Fresh	71.80	72.90	75.23	70.3%	22.4%	7.3%
	Used	71.80	72.90	75.28	64.9%	27.7%	7.4%

Supplemental Figures

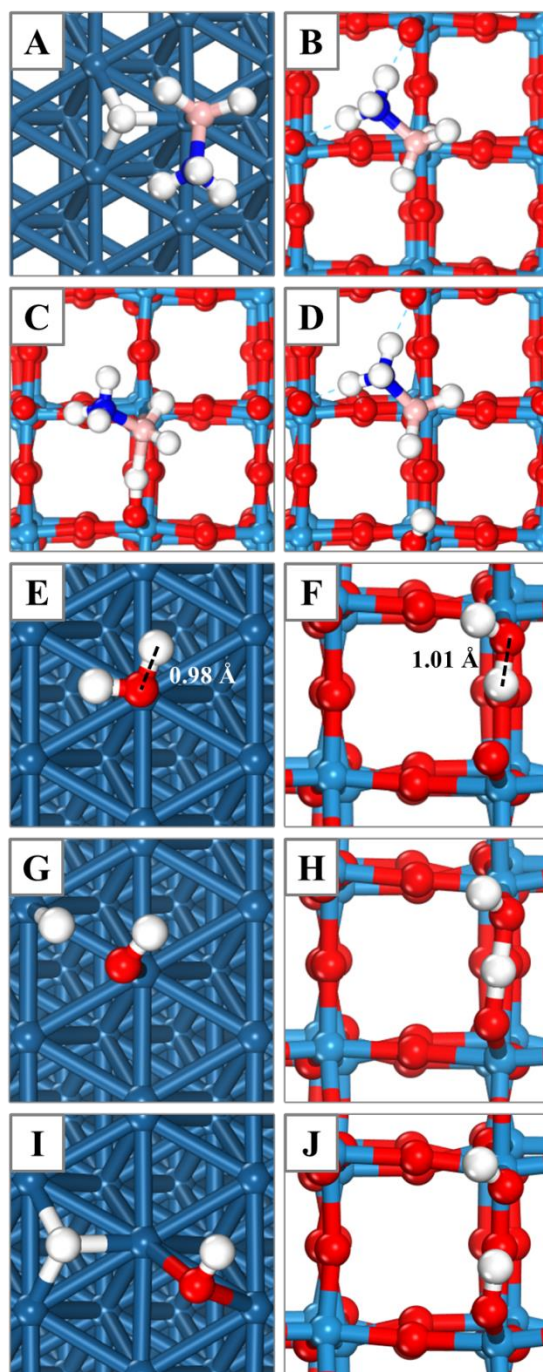


Figure S1. The optimized most stable configurations, related to Figure 1. (A) The final (NH₃BH₂*+H*) state over Pt(111) surface. (B) The initial (NH₃BH₃*), (C) transition (TS) and (D) final (NH₃BH₂*+H*) states over WO₃(100) surface. The (E, F) initial (H₂O*), (G, H) transition (TS) and (I, J) final (HO*+H*) states over Pt(111) and WO₃(100) surface, respectively. Blue, white, red, pink, dark blue and light blue spheres are Pt, H, O, N, B and W atoms, respectively.

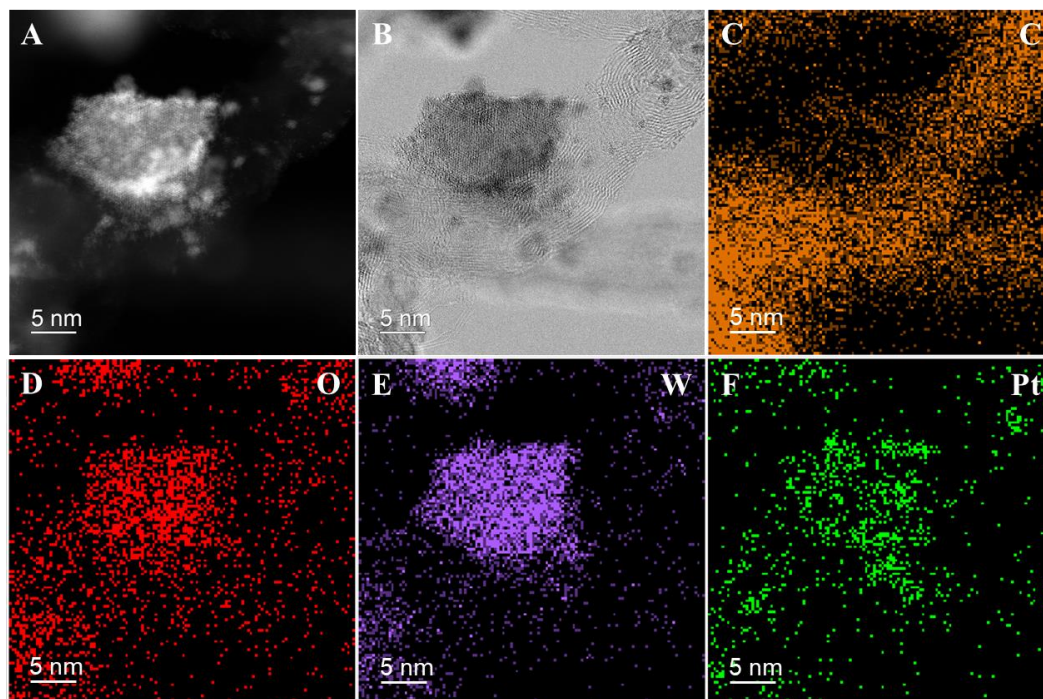


Figure S2. Atomic distribution characterization of Pt/CNT-5W, related to Figure 4. (A) Typical HAADF-STEM image of Pt/CNT-5W. (B) Typical HRTEM image of Pt/CNT-5W. (C-F) The corresponding EDS mappings of C, O, W and Pt elements.

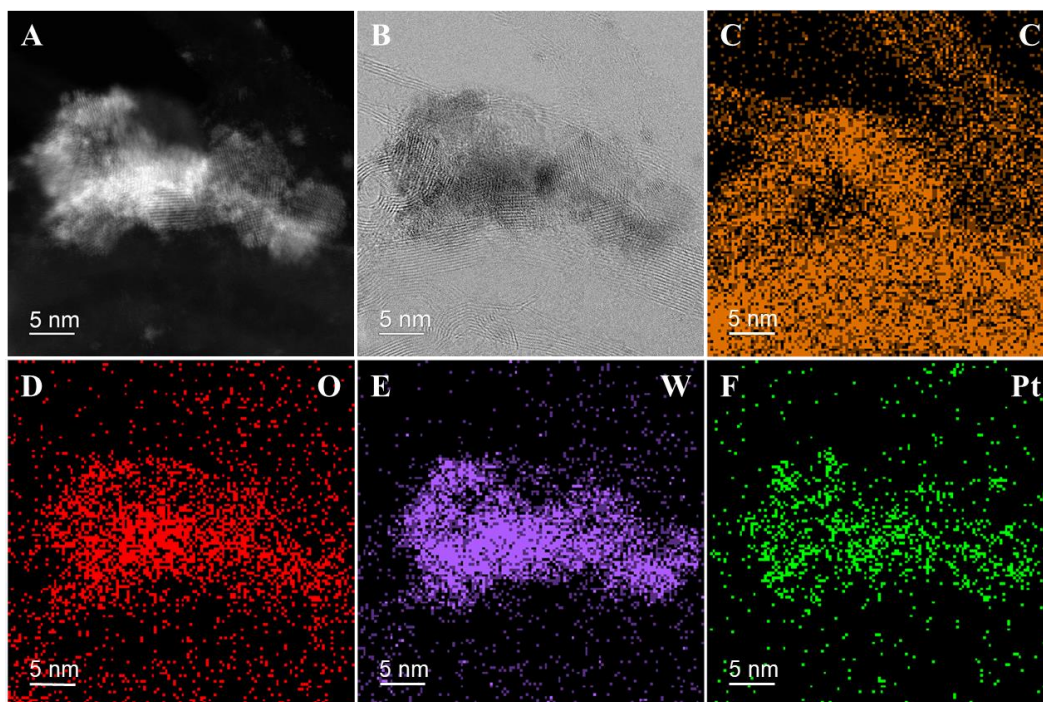


Figure S3. Atomic distribution characterization of Pt/CNT-5W, related to Figure 4. (A)

Typical HAADF-STEM image of Pt/CNT-5W. (B) Typical HRTEM image of Pt/CNT-5W. (C-F)

The corresponding EDS mappings of C, O, W and Pt elements.

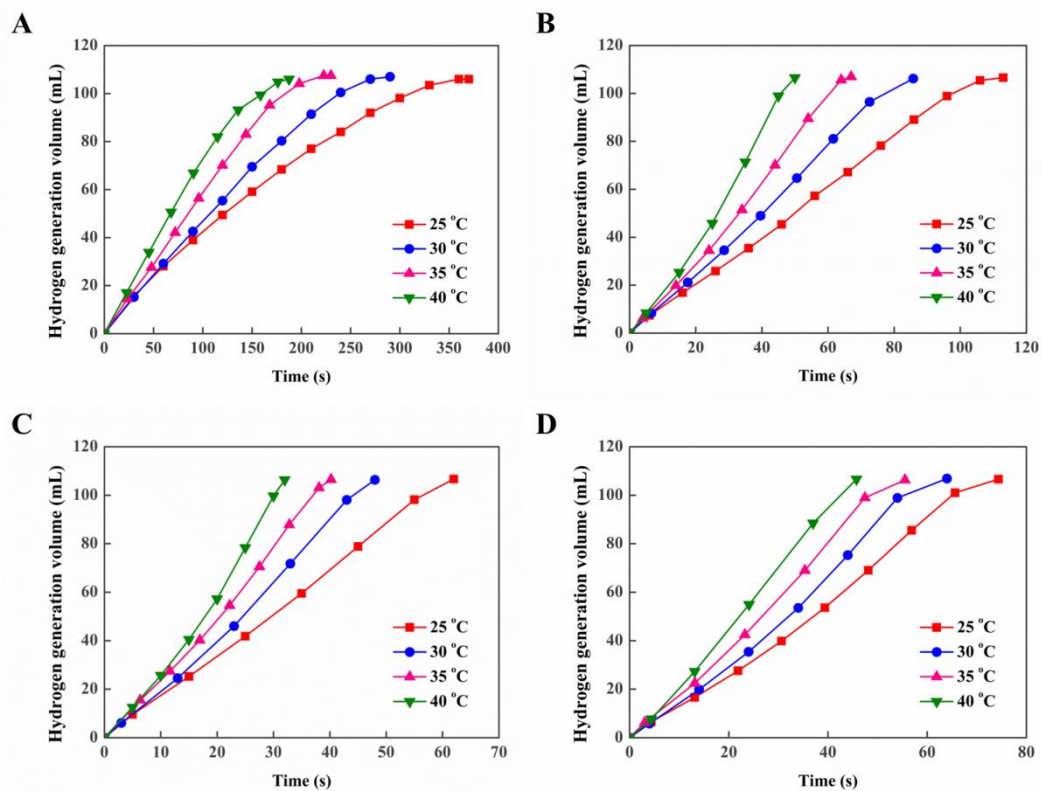


Figure S4. Catalytic activities at different reaction temperatures, related to Figure 6.

Hydrogen generation as a function of time at 25, 30, 35 and 40 °C for (A) Pt/CNT, (B) Pt/CNT-1W, (C) Pt/CNT-5W and (D) Pt/CNT-10W.

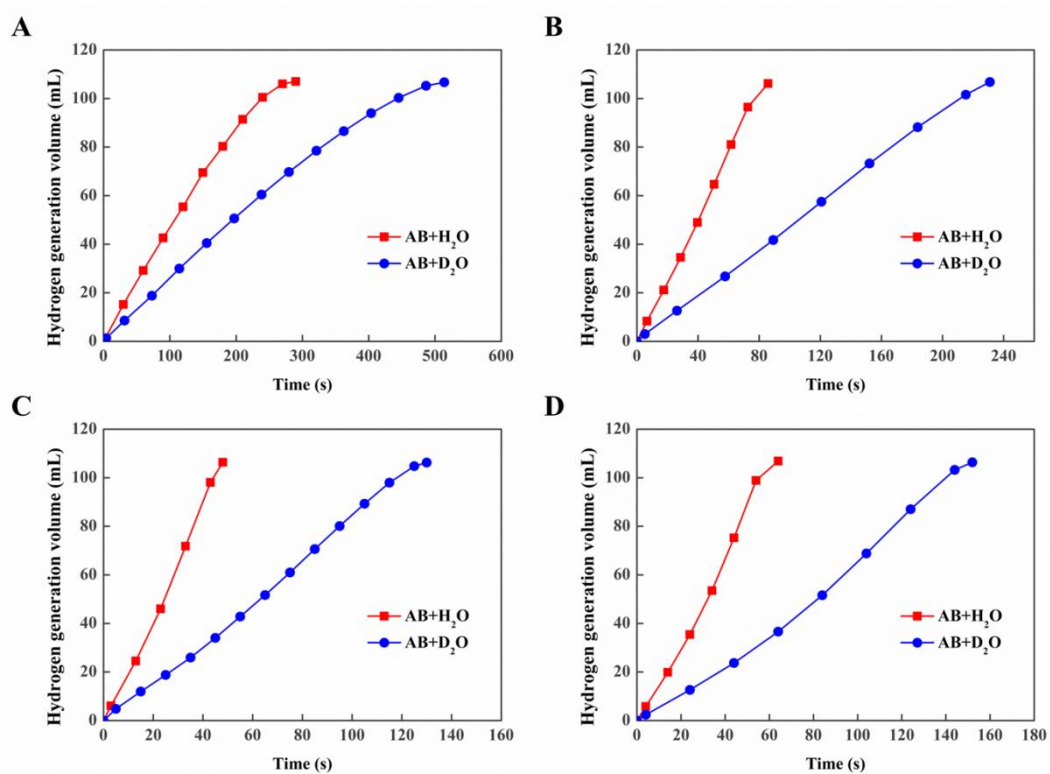


Figure S5. Kinetic isotopic results of the catalysts, related to Figure 6. Hydrogen generation as a function of time by using H₂O and D₂O as reactants at 30 °C for (A) Pt/CNT, (B) Pt/CNT-1W, (C) Pt/CNT-5W and (D) Pt/CNT-10W.

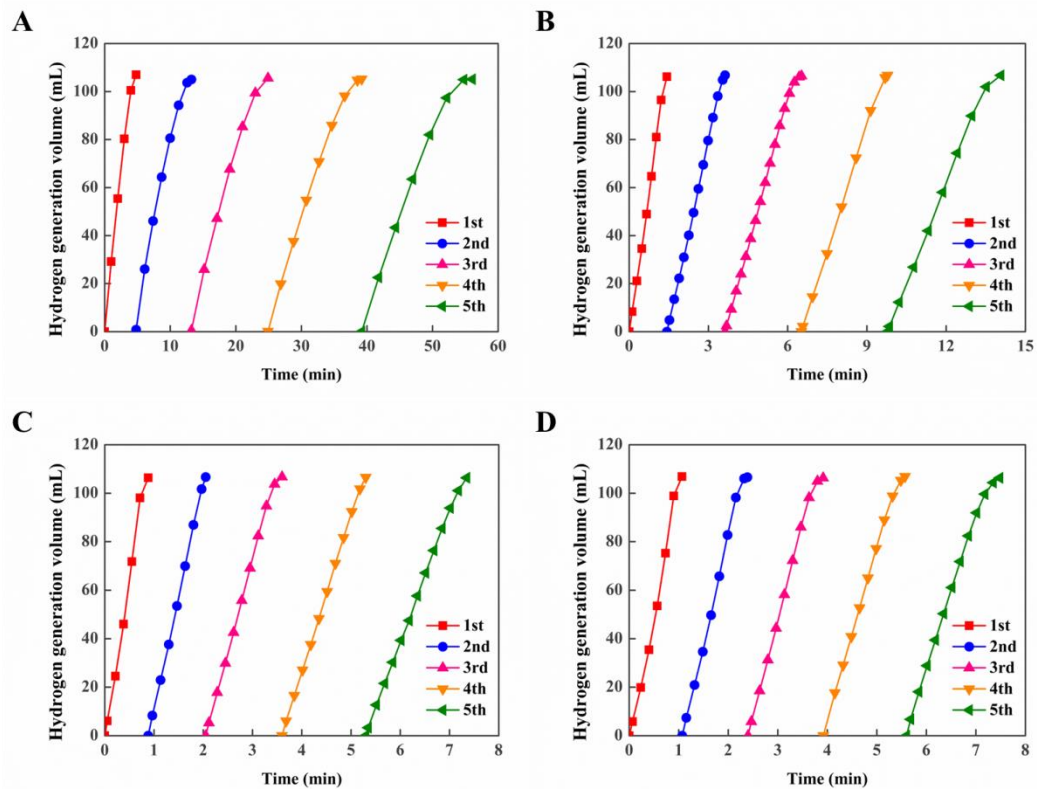


Figure S6. Catalytic durability results of the catalysts, related to Figure 6. Hydrogen generation durability at 30 °C for (A) Pt/CNT, (B) Pt/CNT-1W, (C) Pt/CNT-5W and (D) Pt/CNT-10W.

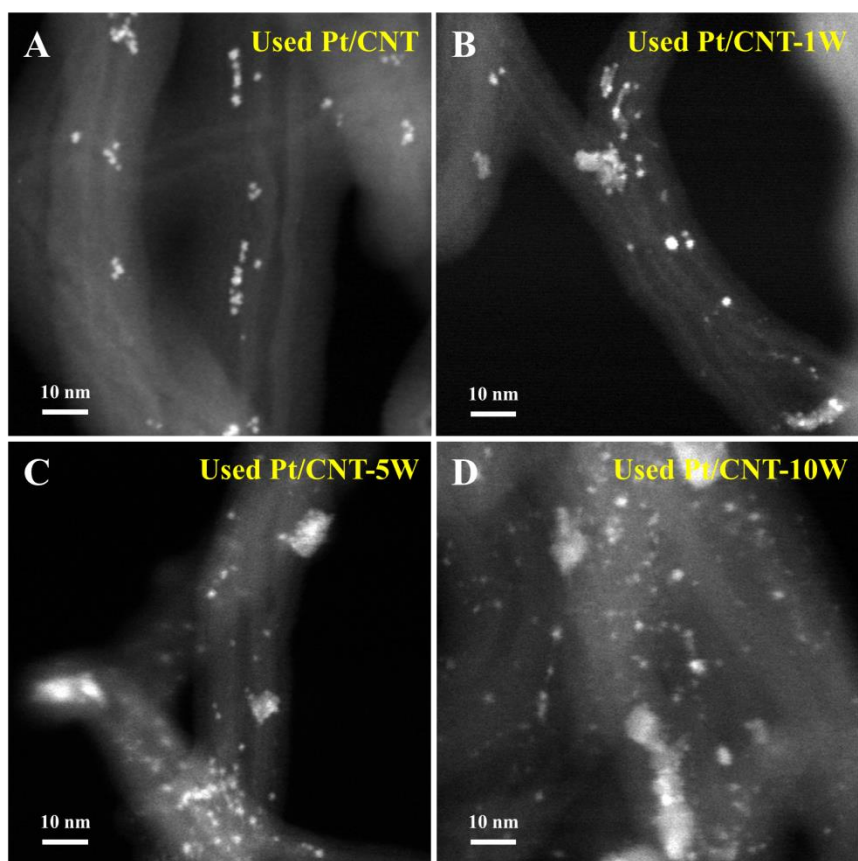


Figure S7. HAADF-STEM characterization of the used catalysts, related to Figure 6. Typical HAADF-STEM images of the used (A) Pt/CNT, (B) Pt/CNT-1W, (C) Pt/CNT-5W and (D) Pt/CNT-10W catalysts.

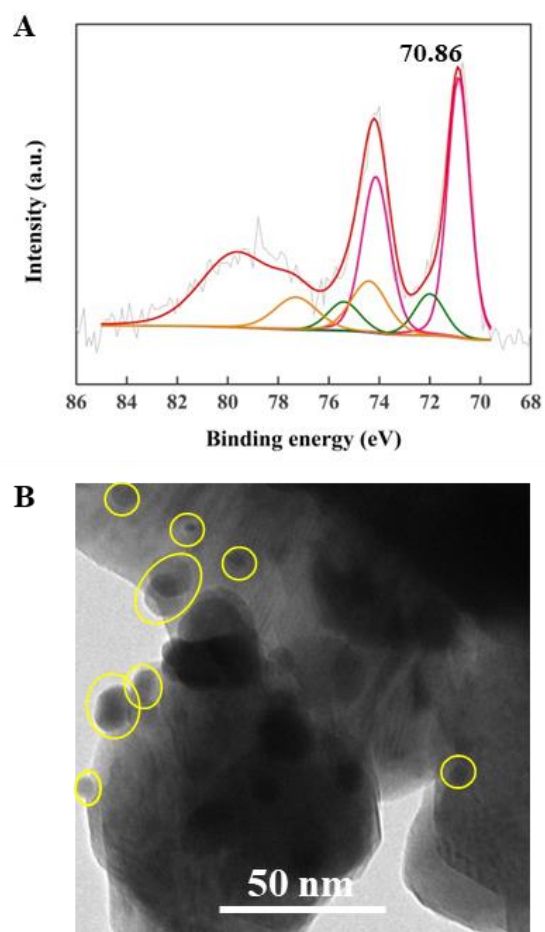


Figure S8. The electronic and structural characterization of Pt/WO₃, related to Figure 6. (A)

XPS Pt 4f spectra and (B) Typical HRTEM image of Pt/WO₃.

Transparent Methods

Catalyst Preparation. Pristine multi-walled carbon nanotubes (CNT, 98%, Beijing Cnano Technology Limited) and WO_3 (99.9%, Adamas Reagent Co., Ltd.) were used as catalyst support. Ammonium tungstate hydrate $((\text{NH}_4)_{10}\text{W}_{12}\text{O}_{41}\cdot x\text{H}_2\text{O}$, 99%, Alfa Aesar) and hexachloroplatinic acid ($\text{H}_2\text{PtCl}_6\cdot 6\text{H}_2\text{O}$, AR, Sinopharm Chemical Reagent Co. Ltd) were utilized as the metal precursors without further purification.

The tungsten-incorporated CNT- γ W supported Pt catalysts were prepared by a two-step method. In the first step, the tungsten-incorporated CNT- γ W hybrid materials were prepared. Typically, a given amount of ammonium tungstate hydrate was dissolved in 20 mL deionized H_2O with an electrical conductivity $<10^{-6}$ S/cm to obtain the solution with different tungsten concentrations of 1, 5 and 10 wt%. Then, 1 g pristine CNT was added into the solution under vigorous agitation, which was maintained at 90 °C for 12 h. After that, the suspension was filtered, washed with deionized H_2O for several times, and dried under stagnant air at 90 °C for 12 h. The as-obtained sample was transferred to a tubular oven and then heated from room temperature to 450 °C with a heating rate of 5 °C \cdot min $^{-1}$ under Ar atmosphere, which was maintained for another 2 h. The resultant tungsten-incorporated CNT- γ W was denoted as CNT- γ W, which γ refers to the concentration of W in the solution. In the second step, pristine CNT, CNT- γ W or WO_3 supported Pt catalysts were prepared by incipient wetness impregnation, which the supports were mixed with an aqueous solution of H_2PtCl_6 to achieve a Pt loading of 1.5 wt%. The impregnated samples were dried at room temperature and then at 80 °C under stagnant air for 12 h,

respectively. Finally, the catalyst precursors were reduced by pure H₂ with a flow rate of 40 ml·min⁻¹ at 250 °C for 2 h. After the reduction, the catalysts were cooled to room temperature under Ar with a flow rate of 40 ml·min⁻¹, and then passivated by 1% O₂/Ar with a flow rate of 40 ml·min⁻¹ for 20 min. The as-obtained catalysts were denoted as Pt/CNT- γ W.

Characterization. X-ray diffraction (XRD) patterns of these supports were recorded using Rigaku D/Max 2550VB/PC diffractometer (Rigaku, Japan) with Cu K α radiation. Thermogravimetric analysis (TGA) of these supports were conducted using TA SDT Q600 analyzer (TA Instruments Co., USA) from room temperature to 800 °C with a heating rate of 10 °C·min⁻¹ under a constant air flow. Raman spectra were recorded using a LabRAM-HR instrument (Horiba Jobin Yvon, France) with an Ar laser (514 nm) for excitation. Hydrogen temperature programmed reduction (H₂-TPR) was carried out in an Autochem 2920 instrument (Micromeritics, USA) with a flow of 10% H₂/Ar (30 mL·min⁻¹) from room temperature to 900 °C with a heating rate of 10 °C·min⁻¹. High angle annular dark field scanning transmission electron microscopy (HAADF-STEM) imaging and energy dispersive X-ray spectroscopy (EDS) elemental mapping were performed by a F20 S-TWIN high-resolution transmission electron microscope (Tecnai G2, FEI Co. USA) with an accelerating voltage of 200 kV. High resolution transmission electron microscopy (HRTEM) observation was performed with a JSM-2100 electron microscope (JEOL, Japan). X-ray photoelectron spectra (XPS) were recorded using Kratos XSAM 800 photoelectron spectrometer

(Manchester, UK) with an Al-K α X-ray source ($h\nu=1486.6$ eV). Inductively coupled plasma atomic emission spectrometer (ICP-AES) analysis was conducted using a 725-ES instrument (Agilent Technologies, USA).

Catalytic Testing. The apparatus used for catalytic activity test of ammonia borane hydrolysis was similar to that previously reported. Typically, prior to the reaction, a given amount of catalysts (0.1 g) was preloaded in a 50 mL three-necked flask containing a Teflon-coated stir bar, which was then transferred to a H₂O bath with a magnetic stirrer. The reaction was initialized by injecting an aqueous ammonia borane solution (5 mL, 0.01 g·mL⁻¹) into the reaction flask with a stirring speed of 900 rpm at 30 °C. A glass gas burette filled with H₂O was connected to the reaction flask to measure the amount of discharged H₂O, which could be weighed by an electronic balance and converted to the volume of evolved hydrogen during the reaction. The hydrolysis of ammonia borane was also conducted at various temperatures, i.e., 25, 30, 35 and 40 °C, to calculate the activation energies (E_a) of different catalysts. In order to investigate the kinetic isotope effect, the reaction was also conducted by replacing H₂O with D₂O as the reactant over different catalysts at the same reaction conditions.

In order to evaluate the durability of these catalysts, the reaction was repeated another 4 times by adding the same amount of ammonia borane solution (5 mL, 0.01 g·mL⁻¹) into the reaction flask after the completion of the last cycle. After the durability test, the used catalysts were separated from the spent solution by filtered, washed with deionized H₂O and dried under vacuum at 30 °C for characterization.

DFT Calculations. The calculations were performed with the Vienna ab initio simulation package (VASP) (Kresse and Hafner, 1993, 1994; Kresse and Furthmuller, 1996a, 1996b), implementing the spin-polarized DFT calculations in conjunction with projected augmented wave (PAW) potentials (Blochl, 1994). The exchange correlation functional was described by generalized gradient approximation of Perdew-Burke-Ernzerhof (GGA-PBE) functional (Perdew, 1996). The Kohn-Sham equation was solved using a cut off energy of 450 eV for the plane wave expansion. For Brillouin-zone integration, we used the $3 \times 3 \times 1$ Monkhorst-Pack k-point mesh for the primitive cell (Monkhorst, 1976). The geometry optimization was converged until the residual forces of each atom were less than 0.05 eV/\AA and the total energy differences less than $<10^{-7} \text{ eV}$. For Pt slab model, a $p(3 \times 3)$ supercells with four layers was under test, which the bottom two layers were fixed for the bulk optimization. For WO_3 slab model, a $p(1 \times 1)$ supercells with seven layers was under test, which the bottom four layers were fixed for the bulk optimization. The adsorption energy (E_{ads}) of species (A) on metal surface (M) is defined as $E_{\text{ads}} = E_{\text{A/M, tot}} - E_{\text{M, tot}} - E_{\text{A, tot}}$, which $E_{\text{A/M, tot}}$, $E_{\text{M, tot}}$ and $E_{\text{A, tot}}$ is the total energies of A adsorbed metal surface, clean metal surface, and A in gas phases, respectively. On the other hand, the activation energy (E_a) is defined as $E_a = E_{\text{TS}} - E_{\text{IS}}$, which E_{TS} and E_{IS} is the energy of the transition state (TS) and the most stable initial state (IS), respectively.

Supplementary References

Kresse, G.; Hafner, J. (1993). Ab initio molecular dynamics for liquid metals. *Phys. Rev. B* 47, 558-561.

Kresse, G.; Hafner, J. (1994) Ab initio molecular-dynamics simulation of the liquid-metal-amorphous-semiconductor transition in germanium. *Phys. Rev. B* 49, 14251-14269.

Kresse, G.; Furthmuller, J. (1996) Efficiency of ab-initio total energy calculations for metals and semiconductors using a plane-wave basis set. *Comp. Mater. Sci.* 6, 15-50.

Kresse, G.; Furthmuller, J. (1996) Efficient iterative schemes for ab initio total-energy calculations using a plane-wave basis set. *Phys. Rev. B* 54, 11169-11186.

Bloch, P. E. (1994) Projector augmented-wave method. *Phys. Rev. B* 50, 17953-17979.

Perdew, J. P.; Burke K.; Ernzerhof M. (1996) Generalized gradient approximation made simple. *Phys. Rev. Lett.* 77, 3865-3868.

Monkhorst, H. J.; Pack, J. D. (1976) Special points for Brillouin-zone integrations. *Phys. Rev. B* 13, 5188-5192.